

## Acoustic microscopy—a summary

Andrew Briggs

Department of Materials, University of Oxford, Parks Road, Oxford OX1 3PH, UK

### Abstract

Acoustic microscopy enables one to image the interaction of acoustic waves with the elastic properties of a specimen with microscopic resolution. A lens with good focusing properties on axis can be used for both transmitting and receiving the signal, and an image is formed by scanning the lens mechanically over the specimen. In pressurised superfluid helium with nonlinear coupling to harmonics a resolution of 15 nm has been achieved, but for routine use 2 GHz is the highest practical frequency, which offers a resolution of about 0.7  $\mu\text{m}$ . The information is contained in the way that the acoustic wave is reflected from the specimen. For subsurface imaging, especially in polymer based materials such as composites and electronic packaging, the enhanced depth resolution of a confocal imaging system can be exploited to give good contrast from the plane of interest even when the specimen contains many scatters. In higher stiffness specimens, including most metals, semiconductors and ceramics, a dominant role in the contrast can be played by Rayleigh waves in the surface. If the specimen has a surface layer, then the propagation of the Rayleigh waves is sensitive to the perturbing action of the layer. If the specimen is anisotropic, then there will be dependence on the orientation of the surface and the direction of propagation in it. If there are surface cracks or boundaries, then there will be strong contrast when they scatter the Rayleigh waves. Detailed theory is available to relate the elastic properties of the surface to the contrast, and these enable informed interpretation of the acoustic images to be made, and also provide a foundation for more quantitative acoustic microscopy.

This review was received in September 1991.

**Contents**

	<b>Page</b>
1. Resolution and imaging <i>or</i> How to make a microscope	853
2. A little theory	861
2.1. Bulk waves	861
2.2. Rayleigh waves	861
2.3. Reflection	862
2.4. Contrast theory: $V(z)$	866
3. Some pictures	875
3.1. A variety of features	875
3.2. Thin films on substrates	879
3.3. Anisotropy	886
3.4. Surface cracks and boundaries	895
4. Where next?	904
Acknowledgments	905
References	906

## 1. Resolution and imaging or How to make a microscope

Every physicist is familiar with the equation governing the relationship between the velocity of a wave and its frequency and wavelength,

$$v = f \times \lambda. \quad (1.1)$$

In any far-field microscope, the resolution is determined by the wavelength used. In a confocal microscope the resolution is (Kino 1987)

$$w = \lambda / 2NA. \quad (1.2)$$

The numerical aperture is  $NA = \sin \theta_0$ , where  $\theta_0$  is the semiangle of the lens aperture subtended at the focus. Therefore, if a good enough lens can be made, the resolution of a microscope can be less than a wavelength, and that wavelength can be made smaller by increasing the frequency. In convenient units, the velocity of sound in water is  $1.5 \mu\text{m ns}^{-1}$ . At 2 GHz (which is the practical upper limit for day-to-day acoustic microscopy) this gives a wavelength of  $0.75 \mu\text{m}$ , which is within the range of visible light. So an acoustic microscope working at this frequency can give a resolution comparable with the resolution of a light microscope (Jipson and Quate 1978).

The refractive index for longitudinal acoustic waves passing from fluids to solids exhibits a much greater range than an optical refractive index could. The velocity in most solids is greater than the velocity in most fluids, and so if we adopt the convention that an acoustic refractive index  $n$  is the ratio of the velocity in a fluid to the velocity in a solid, then in most cases  $n$  will be less than unity. The most common material for acoustic microscope lenses is sapphire. The longitudinal wave velocity parallel to the  $c$ -axis is  $11.1 \mu\text{m ns}^{-1}$ , so that the refractive index from water is  $n = 0.135$ . With such a small refractive index it is possible to focus waves with a single lens surface with a high numerical aperture and negligible aberrations.

An acoustic microscope lens is made by grinding a concave spherical cavity in the lens material, opposite a transducer. Plane waves from the transducer are refracted at the lens surface, and brought to a focus in the coupling fluid. As the refractive index (the ratio of the velocity in the fluid to the velocity in the lens) tends to zero, so each ray, initially parallel to the lens axis, is refracted increasingly close to the normal to the spherical surface. In the limit of zero refractive index the refracted rays would be radial, and so would pass through the centre of curvature of the lens surface. In this limit the wavefronts would be spherical and concentric with the lens surface. Whether in terms of rays or waves, the aberrations would be zero. Now, of course, the refractive index is not zero, but it is small. In third-order geometrical optics, the aberrations are proportional to  $n^2$ . The analogous optical case of a single refracting surface is plane waves in air (or *in vacuo*) incident on a convex glass surface, and focused inside the glass, with an effective refractive index  $n = 0.67$ . In the acoustic case the aberrations would be only 4% of what they would be in the optical situation.

Ray optics is at its weakest when dealing with rays passing through a diffraction-limited focus. So a more accurate way to estimate the sharpness of the focus is to calculate the phase aberrations of the wavefronts (Lemons and Quate 1979). In the absence of any aberration the wavefront after passing through the lens would be a

sphere whose centre is at the focus. For a lens of radius of curvature  $r_0$  subtending an angle of  $\theta$ , at the centre of curvature, the difference between such a sphere and the actual wavefront is the aberration

$$W = \frac{r_0}{1-n} \{1 - [1 - 4n(1-n) \sin^2(\frac{1}{2}\theta)]^{1/2} - 2n(1-n) \sin^2(\frac{1}{2}\theta)\} \\ \approx 2r_0 n^2 (1-n) [\sin^4(\frac{1}{2}\theta) + 2n(1-n) \sin^6(\frac{1}{2}\theta)]. \quad (1.3)$$

When  $n = 1$ , corresponding to a lens with no refraction at all, then  $W = 0$ . As  $n$  decreases  $W$  passes through a maximum (which happens to be at  $n \approx 0.67$  for  $\sin \theta = 0.5$ ), and then falls off again, eventually as  $n^2$  for  $n \ll 1$ . In the example given above with  $r = 0.1$  mm,  $\theta = 50^\circ$  and  $n = 0.135$ , the wavefront distortion would be  $W \approx 0.1$   $\mu\text{m}$ . This is less than a tenth of a wavelength in water at 1 GHz, and the wavefront aberrations are even smaller if the focus is taken as a point slightly closer to the lens than the paraxial focus. For light, with  $n = 0.67$ , the wavefront distortion would be 1  $\mu\text{m}$ , which would be quite unacceptable in a good microscope. In an acoustic microscope, even with only a single lens surface the resolution achieved corresponds closely to the diffraction limit.

The small refractive index is also beneficial in achieving a high numerical aperture. From simple geometrical optics the paraxial focus is at

$$q = \frac{r_0}{1-n}. \quad (1.4)$$

With a refractive index of 0.67, the highest theoretical numerical aperture would be 0.33. With  $n = 0.135$ , for a complete hemispherical surface the numerical aperture would be 0.988, and even for a more realistic lens with a spherical cavity that subtended an angle of  $60^\circ$  at the centre of curvature the numerical aperture would be 0.8. This combination of high numerical aperture and negligible aberrations means that it is possible to make an acoustic lens that will give resolution close to a wavelength.

The velocity difference between sapphire and water is beneficial in ensuring that the aberrations were low. But there is a downside to this. Specific acoustic impedance can be defined as minus the ratio of traction to particle displacement velocity (Auld 1973, Kino 1987); it is equal to the product of the density of a material and the acoustic velocity. The common unit of acoustic impedance is the Mrayl, which is  $10^6 \text{ kg m}^{-2} \text{ s}^{-1}$ . For rays incident normally on an interface the reflection and transmission can be found in terms of the impedance by equations identical to those used in electromagnetism; the same equations can be used for rays at an angle to the interface if the characteristic impedance is divided by the cosine of the angle of incidence or refraction. The characteristic impedance of water is 1.5 Mrayl, while the characteristic impedance of sapphire along the  $c$ -axis is 44.3 Mrayl. This means that only 1.8% of the energy of an axial ray would be transmitted in the two directions across the interface, and an even smaller proportion of the energy of a ray passing through the lens nearer to the edge of the aperture. To reduce these losses, a quarterwave matching layer is coated on the lens surface. This should have an impedance as close as possible to the geometric mean of the impedances of the lens and the coupling fluids: for the most accurate quantitative work chalcogenide glass can be tailored to have the correct impedance (Kushibiki *et al* 1981), but for most imaging purposes borosilicate glass is adequate and is much more robust. The matching layer has a role similar to that of the blooming layer on optical lenses, except that on an acoustic lens it is more important because the impedance mismatch is so much greater.

An acoustic microscope lens is illustrated in figure 1. The lens itself is made of sapphire, which gives a combination of high velocity and low losses. The sapphire must be accurately oriented with the crystal *c*-axis parallel to the lens axis, otherwise the acoustic waves would veer off-axis because of anisotropic effects. The bottom surface has a spherical cavity ground in it. The top surface of the sapphire is flat, and on it a transducer is fabricated, accurately opposite the spherical surface, by sputtering a layer of zinc oxide between two layers of gold. Zinc oxide is a II-VI semiconductor with a rather large piezoelectric coupling coefficient: it can be sputtered epitaxially, so that although the film is polycrystalline the piezoelectric properties are rather well aligned perpendicular to the surface. When a radio frequency pulse is applied to the transducer, plane waves are excited which propagate in the sapphire towards the spherical surface opposite. Here the waves are refracted so as to come to a focus. They propagate in the coupling fluid until they are reflected by the specimen. The whole interest of acoustic microscopy lies in understanding the nature of the reflection from the specimen, and we shall come back to that again and again. The waves travel back through coupling fluid and the lens and reach the transducer. There the waves generate an electrical signal that can be detected by appropriate electronic circuitry.

The electronic circuitry is illustrated schematically in figure 2. It uses essentially radar technology to transmit a pulse and then a short time later to measure it with sensitive detection circuitry (Atalar and Hoppe 1986). The acoustic lens has good properties only on-axis. It has not proved possible to develop a good high-resolution

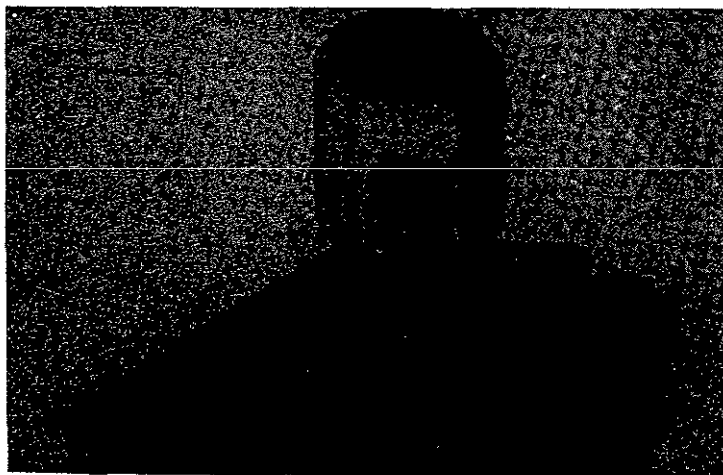


**Figure 1.** A lens for high-resolution acoustic microscopy in reflection. The transparent cylinder is a single crystal of sapphire, with its crystal *c*-axis accurately parallel to the axis of the cylinder. The sandwich structure at the top is the transducer, an epitaxially grown layer of zinc oxide between two gold electrodes. The shaded areas within the sapphire represent the plane wavefronts of an acoustic pulse; they are refracted at the lens cavity so that they become spherical in the coupling fluid. The cavity of a lens for use at 2 GHz has a radius of curvature of 40  $\mu\text{m}$ . (Courtesy of Leica, Wetzlar.)

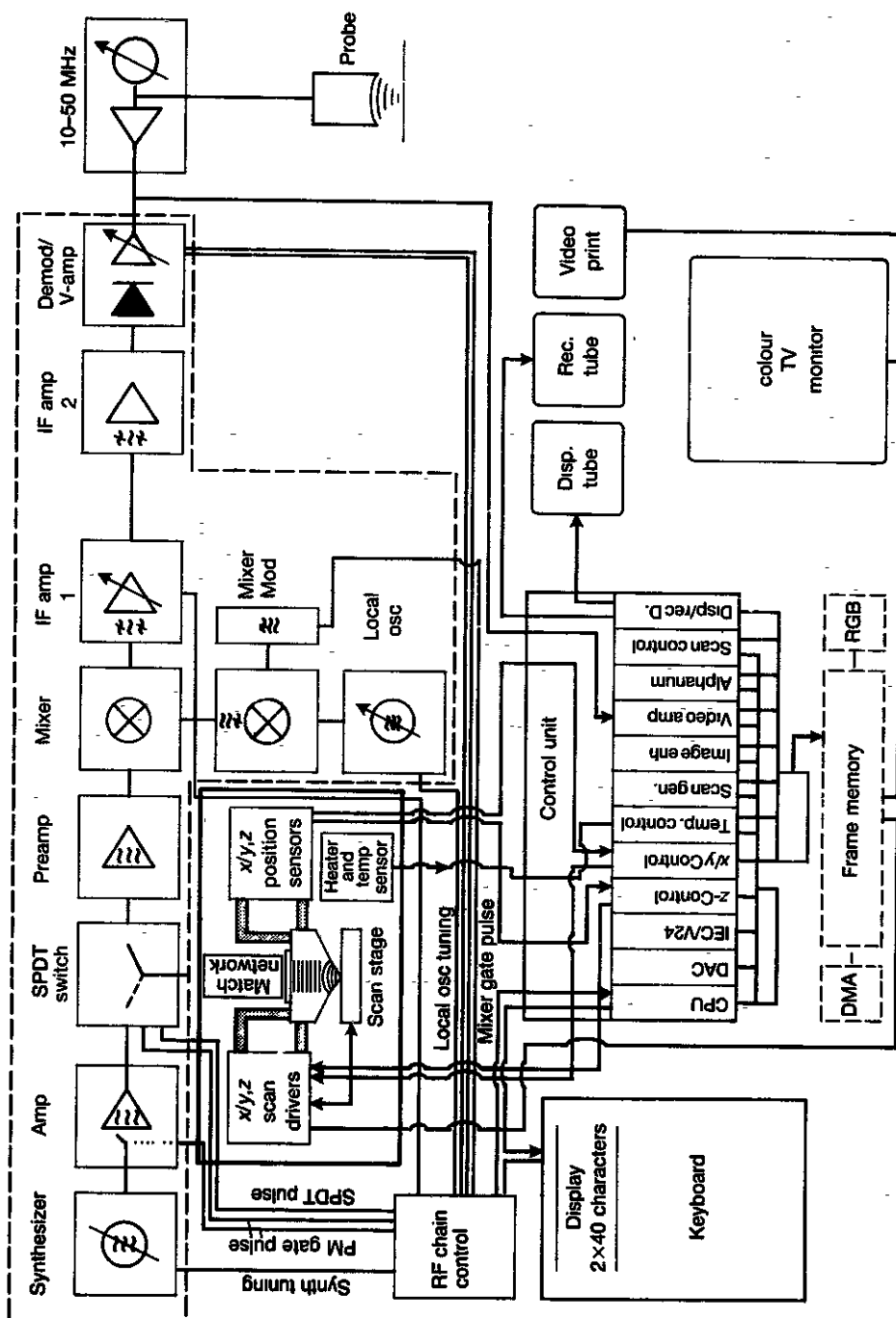


Figure 2. Schematic block diagram of electronics for a reflection acoustic microscope; this microscope also has facilities for low-frequency operation down to 10 MHz, and a video printer hard copy output. (Courtesy of Leica, Wetzlar.)

acoustic lens that has useful properties off-axis, nor to be able to image an extended field of view simultaneously. When the concept of mechanical scanning was introduced for acoustic microscopy (and also for scanning optical microscopy) in the late 1970s, it seemed a bitter pill to swallow. But now mechanical scanning is so familiar that one scarcely gives it a second thought. Much of the control system in figure 2 is given over to controlling the scanning and handling the image data. The mechanical scan itself is usually achieved with leaf springs, with a maximum scan rate of 25 or 50 Hz in the fast scan direction. This means that it takes in the range of 5–40 s to obtain a complete picture, depending on the resolution required. This covers scans of up to a millimetre or so. There is important work to be done using larger scans: for that, slower scanning systems must be used, taking several minutes for a complete picture.

There is no practical limit to the mechanical precision with which the components for the lens and the scanning can be made. Why then can the resolution not be improved indefinitely? In terms of (1.1), why can the frequency not be increased to give an arbitrarily short wavelength? The answer lies in the attenuation of acoustic waves in the coupling fluid. It is easily shown that in a linear viscoelastic fluid the attenuation varies as the square of the frequency. Actually a simple model based on the shear viscosity of a fluid such as water gets the answer wrong by a numerical factor, because there are other relaxation mechanisms operating, but nevertheless the  $f^2$  dependence is indeed borne out experimentally. This  $f^2$  dependence is a very hard wall to hit up against. Suppose that a lens was designed with a cavity radius that would give an attenuation of 40 dB in the fluid when a reflecting object was placed at its focus (a quantity in units of decibels is 10 times the logarithm to base 10 of the ratio of two powers, in this case the transmitted signal and the return signal), and that this gave a signal-to-noise ratio at the receiving amplifier of 20 dB. If you tried to gain an improvement of a factor of two in the resolution of the lens, by doubling the frequency, then attenuation would increase by a factor of four to 160 dB, and the signal would be -100 dB, or a factor of  $10^{10}$  in power, below the noise. No amount of signal processing would enable you to extract that signal. So to improve the resolution with a given coupling fluid, the radius of the lens cavity must be reduced as the frequency is increased.

The limitation on how small the cavity can be is not, curiously enough, determined by how small a cavity can be ground. It is rather determined by how short the pulses can be. However good the matching layer on the lens is, there will always be some reflection from the lens-water interface, and inevitably this may be comparable in magnitude with the reflection from the specimen, which has suffered the attenuation in the coupling fluid. So the reflection from the lens surface must be sufficiently separated in time from the reflection from the specimen that the two do not overlap. This is determined in turn by two factors, the speed of the radio frequency switches and the bandwidth of the transducer. Although a radius of curvature of 15  $\mu\text{m}$  has been successfully used with water as the coupling fluid (Hadimioglu and Quate 1983), 40  $\mu\text{m}$  is the smallest that is sensible for routine use, corresponding to a time interval of 60 ns between the lens echo and the specimen echo. With this radius of curvature, and therefore a round-trip distance in the water of about 90  $\mu\text{m}$ , the maximum frequency that can be used with water as the coupling fluid is 2 GHz, giving the 0.75  $\mu\text{m}$  wavelength. But is water the only candidate for the coupling fluid?

Other candidates for coupling fluids have been considered exhaustively (Attal and Quate 1976, Lemons and Quate 1979). Organic solvents have a relatively high viscosity. Methanol alone has a viscosity low enough for the performance to be even comparable

with water, and although for most purposes it is not as good as water it is sometimes used when a lower velocity is necessary. Other organic fluids can be useful for acoustic microscopy below the freezing point of water (Yamanaka *et al* 1989). Liquid metals, such as mercury and gallium, are poisonous and can destroy metal specimens. Gallium also oxidizes rather rapidly, and the only successful experiment with gallium as the coupling fluid was so difficult that it has never been repeated (Jipson 1979). Mercury continues to be used occasionally (Attal 1980, Attal *et al* 1989). Gases at high pressure have been tried, but the experiments were discontinued (Wickramasinghe and Petts 1980). Cryogenic liquids alone offer the potential of better resolution than water (Heiserman 1980). In the end, there are only two fluids that offer significantly better resolution than cold water. One is hot water. The attenuation in water at 20 °C is  $0.226 \text{ dB } \mu\text{m}^{-1} \text{ GHz}^{-2}$ , whereas at 60 °C it is  $0.086 \text{ dB } \mu\text{m}^{-1} \text{ GHz}^{-2}$ , a factor of 2.6 smaller. In all high-resolution water-coupled acoustic microscopy the water is therefore heated. The other competitor is superfluid helium.

Acoustic microscopy with helium as the coupling fluid uses a dilution refrigerator to cool the helium to 0.2 K or below (Foster and Rugar 1983, Hadimioglu and Foster 1984). At these temperatures viscosity and thermal conductivity contribute less and less to the attenuation, which then becomes due only to much weaker phonon scattering-processes and varies only linearly with the frequency. Attenuation in the coupling fluid is then no longer a limiting factor, and from that point of view the frequency can be increased with ease. But two other problems remain: the acoustic mismatch between sapphire and helium is far greater than between sapphire and water, and the quarter wave matching layer is correspondingly both more crucial and more difficult to get right; and there is also a severe difficulty in matching the transducer impedance to a 50  $\Omega$  line, because of the very small capacitive impedance when the transducer is thin and the frequency is high. The low velocity and impedance of helium also mean that there is depletion into harmonics at relatively low intensities; this means that only modest pulse powers can be used, and therefore that the receiving amplifier must itself be cooled to liquid helium temperatures in order to give an adequate ratio of signal to thermal noise. These formidable problems have been overcome, and beautiful pictures of bacteria and electronic devices have been obtained at 8 GHz. Since the velocity of acoustic waves in helium at these temperatures is only  $0.238 \text{ } \mu\text{m ns}^{-1}$ , this frequency gives a resolution of 30 nm. It has even been possible to image the scattering of phonons by internal structure in a solid (Foster and Rugar 1985). If ballistic phonons are generated by a heater on the back face of a specimen, then when they reach the front surface they can scatter the frequency of incident acoustic waves out of the bandwidth of a microscope detection system. Regions of the surface on which phonons from the heater are incident will therefore appear dark.

By raising the pressure of the liquid helium to 2 MPa (20 atm) or above, even phonon scattering can be eliminated, and this is how the highest resolution acoustic images have been obtained (Muha *et al* 1990). An example is shown in figure 3. The specimen was a titanium grating with a 20 nm period on a silicon substrate. For comparison, a scanning electron micrograph is shown, taken at 5 keV with 10 nm carbon coating to reduce charging. The acoustic micrograph, taken before the carbon coating, was at a pressure of 2.14 MPa and a temperature of 0.4 K. The frequency was 15.3 GHz, and the resolution was estimated to be 15 nm. This is the highest resolution ever achieved by acoustic microscopy.

One of the most fascinating phenomena to have emerged from the low-temperature studies is nonlinear enhancement of resolution. The effect is illustrated by images at



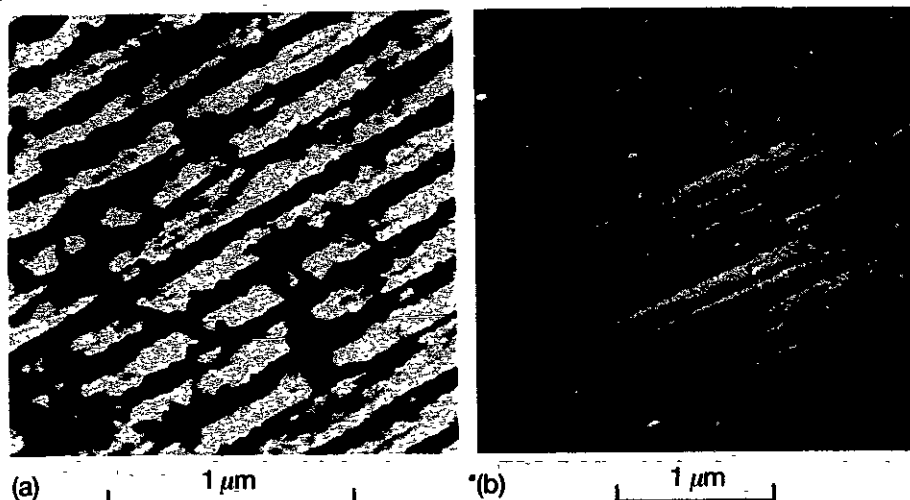
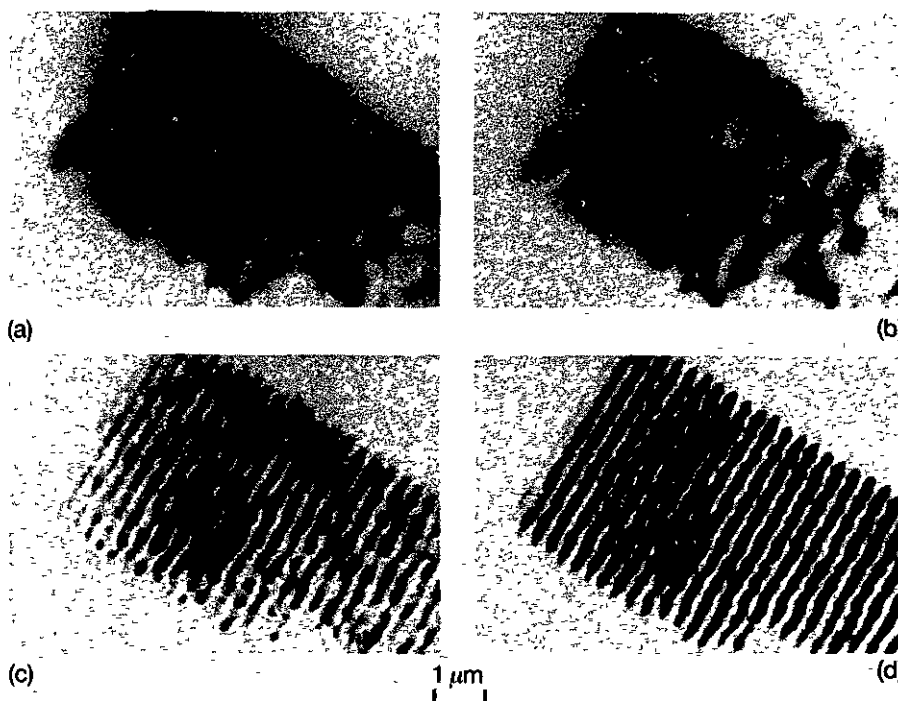


Figure 3. The highest resolution ever achieved by acoustic microscopy, a 200 nm period titanium grating on a silicon substrate (a) acoustic, using pressurized superfluid helium at 0.4 K and 2.14 MPa, 15.4 GHz; (b) SEM, coated with 10 nm carbon, 5 keV. (Courtesy of Michael Muha.)

increasing intensities of a grating in liquid nitrogen in figure 4. Nonlinear enhancement of resolution has also been demonstrated in superfluid  $^4\text{He}$  at 370 MHz (Karaki *et al* 1991). When the changes in pressure associated with the propagation of a wave become sufficiently large, they lead to corresponding changes in the density and bulk modulus over a wavelength. The wave travels faster at the peaks in the pressure in each cycle and slower at the troughs. The wave becomes distorted into a sawtooth waveform (Bjørnø and Lewin 1986). The higher harmonics have shorter wavelengths associated with them than the fundamental, and so the diffraction limit to the resolution should be correspondingly better for the harmonics. When the wave passes through the focal region there is a phase change of  $\pi$  (Born and Wolf 1980), and so the shape of the waveform is reversed. The faster speed of the pressure peaks now leads to a distortion of the sawtooth waveform back to a more sinusoidal waveform. This implies a conversion of energy from the higher harmonics, which contain information with spatial resolution better than the diffraction limit associated with the fundamental frequency, back to the fundamental frequency at which they can propagate through the coupling fluid and be detected at the transducer. Perhaps the most astonishing aspect is that the information obtained at the higher frequency is converted back to the lower frequency so that it can be carried back to the lens. The resolution associated with the second harmonic is better by a factor of  $\sqrt{2}$  compared with the resolution of the fundamental beam. The reason for this can be visualized by assuming a Gaussian profile and considering two extreme cases. If all the second harmonic were excited in the focal plane, then the amplitude profile of the harmonic would follow the intensity profile of the fundamental, which in turn would have a width (however defined)  $1/\sqrt{2}$  of the width of the amplitude profile of the fundamental. The other extreme is that the harmonic is excited well away from the region of the focal phase change. Now the wavelength is half the fundamental wavelength, but then the size of the aperture



**Figure 4.** A 290 nm gold grating on silica in liquid nitrogen, with  $\lambda_0 = 430$  nm at 2.0 GHz, at increasing levels of peak power to the transducer: (a) 10 mW, (b) 32 mW; (c) 100 mW, (d) 320 mW (Foster and Rugar 1985)

of excitation is again  $1/\sqrt{2}$  of the fundamental beam width at any point, by an argument similar to that in the focal plane. So once again the diffraction spot size is  $1/\sqrt{2}$  smaller. The reality must lie somewhere between these two cases.

Although cryogenic liquids show nonlinear effects more easily, nonlinear resolution enhancement can also be seen in water. The highest resolution images with water as the coupling fluid used a frequency of 4.2 GHz, and gave a resolution of  $0.2 \mu\text{m}$  (Hadimioglu and Quate 1983). But most practical microscopy is done at frequencies of 2 GHz and below in order to allow sufficient flexibility in the imaging conditions to reveal information about the elastic properties of the specimen. And this is why water is chosen for the coupling fluid for the vast majority of acoustic microscopy. The impedance and velocity mismatch of liquid helium to most solids is simply too great, so that the acoustic waves just bounce off the surface; this is equivalent to the Kapitza resistance that makes heat transfer so difficult between liquid helium and a solid in cryogenic experiments. And it is the ability to image elastic properties, rather than the resolution alone, that gives acoustic microscopy its unique role. With water as the coupling fluid it is possible to couple into bulk waves in low-velocity and impedance materials, such as biological tissue and polymers, and it is also possible to couple into surface waves, or Rayleigh waves, in most higher stiffness materials, such as metals, ceramics and semiconductors. In order to see how these can give information about the elastic properties, it may be helpful to summarize a little elementary theory.

## 2. A little theory

### 2.1. Bulk waves

In a fluid sound propagates as a longitudinal wave with velocity

$$v_0 = \sqrt{(B/\rho)} \quad (2.1)$$

where  $B$  is the adiabatic bulk modulus and  $\rho$  is the density. A solid can support shear stresses as well as longitudinal stresses, and so in an isotropic solid there can be both a longitudinal wave, with velocity

$$v_l = \sqrt{(c_{11}/\rho)} \quad (2.2)$$

and two polarizations of shear wave, each with velocity

$$v_s = \sqrt{(c_{44}/\rho)}. \quad (2.3)$$

The tensor elastic stiffness constants are related to the Young modulus  $E$  and the shear modulus  $\mu$  by the relationships  $c_{11} \equiv \mu(4\mu - E)/(3\mu - E)$  and  $c_{44} \equiv \mu$ . In anisotropic solids, such as single crystals or composites, there are still three orthogonal waves, but in general the degeneracy of the shear waves is lifted and the waves are no longer pure longitudinal or shear.

### 2.2. Rayleigh waves

A key role in acoustic microscopy is played by Rayleigh waves. These are surface acoustic waves whose existence was discovered theoretically by Lord Rayleigh in 1885 (Rayleigh 1885), and whose centenary was celebrated in 1985 (Ash and Paige 1985; Auld 1985). Rayleigh waves consist of a mixture of longitudinal and shear waves, and they have a component of wavevector parallel to the surface  $\beta$  that is greater than both the longitudinal and shear bulk wavenumbers  $k_l$  and  $k_s$ . Therefore, to satisfy Pythagoras' theorem both the longitudinal and the shear component waves must have components of wavevector normal to the surface  $\alpha_l$  and  $\alpha_s$  that are pure imaginary, so that the waves decay into the bulk. These requirements may be written

$$\beta^2 + \alpha_l^2 = k_l^2 \quad (2.4)$$

$$\beta^2 + \alpha_s^2 = k_s^2. \quad (2.5)$$

With the further requirement that the components of surface traction are all zero, an equation for the velocity of the Rayleigh wave can be derived,

$$4\beta^2 \alpha_l \alpha_s + (-\alpha_s^2 + \beta^2)^2 = 0. \quad (2.6)$$

By substituting for the Rayleigh wavenumber  $\beta$  in terms of the Rayleigh velocity  $v_R$  and the frequency  $\omega$ ,  $\beta \equiv \omega/v_R$ , and similarly for the bulk wavenumbers in (2.4) and (2.5), the Rayleigh velocity can be expressed in a sextic equation,

$$\left(\frac{v_R}{v_s}\right)^6 - 8\left(\frac{v_R}{v_s}\right)^4 + 8\left[3 - 2\left(\frac{v_s}{v_l}\right)^2\right]\left(\frac{v_R}{v_s}\right)^2 - 16\left[1 - \left(\frac{v_s}{v_l}\right)^2\right] = 0. \quad (2.7)$$

This equation has only one root that is real and positive.

The value of the Rayleigh velocity depends primarily on the shear wave velocity of the material. In terms of the Poisson ratio  $\sigma$ , (2.7) takes the form

$$\frac{X^3}{8(1-X)} + X = \frac{1}{1-\sigma} \quad (2.8)$$

where  $X = (v_R/v_s)^2$ . For the permissible range of  $\sigma$  from 0 to 0.5, over which  $v_s/v_l$  ranges from  $1/\sqrt{2}$  to 0,  $v_R/v_s$  lies in the range 0.87–0.96, although at the limit  $\sigma = 0.5$  both the shear and the Rayleigh velocities vanish. An approximate solution to (2.8) is (Scruby *et al* 1987)

$$v_R \approx v_s(1.144\,18 - 0.257\,71\sigma + 0.126\,61\sigma^2)^{-1}. \quad (2.9)$$

The longitudinal and shear wave components decay exponentially into the solid, the longitudinal component decaying rather faster. Like the ratio of the velocity to the shear velocity, the rates of decay depend on the Poisson ratio, but only weakly. A characteristic depth for the stress profile of the Rayleigh wave can be defined as

$$z_c = i \frac{\alpha_l + \alpha_s}{\alpha_l \alpha_s} \quad (2.10)$$

remembering that  $\alpha_l$  and  $\alpha_s$  are pure imaginary. For the whole range of Poisson ratio from 0 to 0.5,  $z_c$  varies only from  $0.53\lambda_R$  to  $0.70\lambda_R$ , where  $\lambda_R$  is the Rayleigh wavelength. In contrast that is dominated by the excitation of Rayleigh waves in a specimen, we may consider the acoustic microscope to be probing that depth of the surface.

### 2.3. Reflection

Acoustic impedance has already been introduced in section 1 as minus the ratio of traction  $\sigma_T$  to particle displacement velocity  $\partial u/\partial t$ , which is equal to the product of the density and the acoustic velocity,

$$Z \equiv -\frac{\sigma_T}{\partial u/\partial t} = \rho v. \quad (2.11)$$

For normal incidence at an interface between media 1 and 2, the stress amplitude reflection and transmission coefficients  $R$  and  $T$  can then be written directly in terms of the impedance of each medium,

$$R = \frac{Z_2 - Z_1}{Z_2 + Z_1} \quad (2.12)$$

$$T = \frac{2Z_2}{Z_2 + Z_1}. \quad (2.13)$$

At a general angle of incidence, Snell's law is obeyed:

$$\frac{\sin \theta_1}{\sin \theta_2} = \frac{v_1}{v_2}. \quad (2.14)$$

Snell's law is equivalent to requiring the component of the wavevector parallel to the interface to be continuous. Calculation of the reflection and transmission coefficients for oblique incidence is complicated by the fact that three waves can be excited in each medium. A particularly important situation for acoustic microscopy is the case of waves from a fluid incident on a solid. In this case there is one reflected wave in the fluid (denoted by no subscript) and, in an isotropic solid, two transmitted waves, one longitudinal (subscript l) and one shear polarized in the plane of incidence (subscript s; the other shear polarization is not excited). Snell's law in this situation is

$$\beta = k \sin \theta = k_l \sin \theta_l = k_s \sin \theta_s \quad (2.15)$$

Of the six boundary conditions (continuity across the boundary of three components of displacement and three components of traction), those concerned with displacement and stress in the  $y$ -direction are not relevant, nor is displacement in the  $x$ -direction since the fluid can slide freely. Hence the boundary conditions are continuity of displacement and traction normal to the surface, and zero traction parallel to the surface. Defining the normal impedances, with the densities of the fluid and the solid as  $\rho_0$  and  $\rho_1$ ,

$$Z = \frac{\rho_0 v_0}{\cos \theta} \quad Z_1 = \frac{\rho_1 v_1}{\cos \theta_1} \quad Z_s = \frac{\rho_1 v_s}{\cos \theta_s} \quad (2.16)$$

the pressure or stress amplitude reflection and transmission coefficients are

$$R(\theta) = \frac{Z_1 \cos^2 2\theta_s + Z_s \sin^2 2\theta_s - Z}{Z_1 \cos^2 2\theta_s + Z_s \sin^2 2\theta_s + Z} \quad (2.17)$$

$$T_1(\theta) = \frac{2Z_1 \cos 2\theta_s}{Z_1 \cos^2 2\theta_s + Z_s \sin^2 2\theta_s + Z} \quad (2.18)$$

$$T_s(\theta) = \frac{-2Z_s \sin 2\theta_s}{Z_1 \cos^2 2\theta_s + Z_s \sin^2 2\theta_s + Z} \quad (2.19)$$

By making the substitution

$$Z_{\text{tot}} = Z_1 \cos^2 2\theta_s + Z_s \sin^2 2\theta_s \quad (2.20)$$

the reflectance function can be written in the form

$$R(\theta) = \frac{Z_{\text{tot}} - Z}{Z_{\text{tot}} + Z} \quad (2.21)$$

which is already familiar from (2.12).

Finally, the reflectance function can also be written explicitly in terms of the wavenumber in the fluid  $k$  and the longitudinal and shear wavenumbers in the solid  $k_1$  and  $k_s$ , and the tangential component of the wavevector  $\beta = k_x$ , which, by Snell's law, is the same in both media, and the densities of the fluid and the solid  $\rho_0$  and  $\rho_1$  (Bertoni and Tamir 1973),

$$R(k_x) = \frac{[(2k_x^2 - k_s^2)^2 - 4k_x^2 \sqrt{(k_x^2 - k_1^2)(k_x^2 - k_s^2)}] - ik_s^4 \sqrt{(k_x^2 - k_1^2)(k_x^2 - k_s^2)} \rho_1 / \rho_0}{[(2k_x^2 - k_s^2)^2 - 4k_x^2 \sqrt{(k_x^2 - k_1^2)(k_x^2 - k_s^2)}] + ik_s^4 \sqrt{(k_x^2 - k_1^2)(k_x^2 - k_s^2)} \rho_1 / \rho_0} \quad (2.22)$$

If  $k_x$  is regarded as a complex component of wavevector, with the imaginary part representing an exponential decay in intensity, then (2.22) will give poles and zeros of  $R(k_x)$  in the complex plane at  $k_x = \pm k_p$  and  $k_x = \pm k_0$  respectively. The behaviour in the vicinity of the poles and zeros can be approximately described by a term of the form  $(k_x^2 - k_0^2)/(k_x^2 - k_p^2)$ . If the behaviour of the remainder of the reflectance function is described by the function  $R_0(k_x)$ , then

$$\begin{aligned} R(k_x) &\equiv R_0(k_x) \frac{k_x^2 - k_0^2}{k_x^2 - k_p^2} = R_0(k_x) \left( 1 + \frac{k_p^2 - k_0^2}{k_x^2 - k_p^2} \right) \\ &\approx R_0(k_x) + \frac{k_p^2 - k_0^2}{k_x^2 - k_p^2} \end{aligned} \quad (2.23)$$

The approximation in the second line is a good one, because in the vicinity of the pole (specifically beyond the shear critical angle in figure 5 below)  $R_0(k_x) = 1$ . The benefit of this analysis is that it separates the component of the reflection that is associated with the excitation of Rayleigh waves from everything else. The real part of  $k_p$  is  $2\pi/\lambda_R$ , where  $\lambda_R$  is the Rayleigh wavelength, and the imaginary part is the exponential decay. The total Rayleigh wave attenuation per unit distance,  $\alpha_T$ , may contain contributions from elastic scattering, inelastic damping, and leaking into the coupling fluid. If the attenuation is due solely to radiation into the fluid, then  $k_0$  is the complex conjugate of  $k_p$ . The attenuation due to leaking into the coupling fluid,  $\alpha_R$ , may be calculated approximately from (Dransfeld and Salzmänn 1970)

$$\alpha_R \lambda_0 \approx \frac{\rho_0 v_0^2}{\rho_1 v_R^2} = \frac{\rho_0}{\rho_1} \sin^2 \theta_R \quad (2.24)$$

where  $\rho_0$  and  $\rho_1$  are the densities of the fluid and the solid, and  $\theta_R$  is the Rayleigh angle as usual. The value of (2.24) has the form of a ratio of impedances multiplied by a ratio of velocities, and it provides a means of relating Rayleigh wave attenuation (due to radiation into the fluid) to the density of the specimen. Provided that the fluid loading is light (as it is in almost all acoustic microscopy in which Rayleigh wave contrast is important), then the imaginary part of  $k_0$  is much smaller than the real part, and the magnitude of the reflectance function is unity throughout the range of incident angle over which the phase change associated with the Rayleigh pole occurs. The final approximation in (2.23) enables certain integrals to be achieved analytically in the ray theory of contrast, and the theory of contrast from cracks.

In a small number of materials of intermediate stiffness (mainly polymers of relatively high moduli such as polymethyl methacrylate (PMMA)) lateral longitudinal waves can take the place of Rayleigh waves, so that the longitudinal critical angle replaces the Rayleigh angle in calculating the period of the oscillations. In this case the dominant effect comes from the branch point singularities at  $\pm k_1$  due to the terms in  $\kappa_1 = \sqrt{(k_x^2 - k_1^2)}$  in (2.22). The lateral longitudinal contribution in the reflectance function can be separated from the rest in a manner analogous to (2.24), by expanding the reflectance function to first order in  $\kappa_1/k_1$  (Chan and Bertoni 1990);

$$R(k_x) \equiv A(k_x) + B(k_x)\kappa_1/k_1. \quad (2.25)$$

In the vicinity of  $k_1$ , to first approximation the values of  $A(k_x)$  and  $B(k_x)$  may be taken as their values at  $k_x = k_1$ , which are

$$A(k_1) = 1$$

$$B(k_1) = -2 \left( \frac{c_{11}}{c_{12}} \right)^2 \frac{\rho_0}{\rho_1} \tan \theta_1. \quad (2.26)$$

Two sets of curves of stress amplitude functions  $R(\theta)$ ,  $T_l(\theta)$  and  $T_s(\theta)$  calculated from (2.17) to (2.19) are shown in figure 5. The reflection and transmission coefficients are complex-valued functions: in these figures the modulus is shown by the full curve and the phase is shown by the broken curve. The curves in figure 5(a) are for waves incident from water on PMMA. At normal incidence, only a longitudinal wave is excited in the solid, so the reflection coefficient is simply  $R = (Z_1 - Z_0)/(Z_1 + Z_0)$ , the longitudinal transmission coefficient is  $2Z_0/(Z_1 + Z_0)$ , and the shear transmission coefficient is zero. As the angle of incidence increases, both longitudinal and shear waves are excited in the solid, until the critical angle for excitation of longitudinal waves is

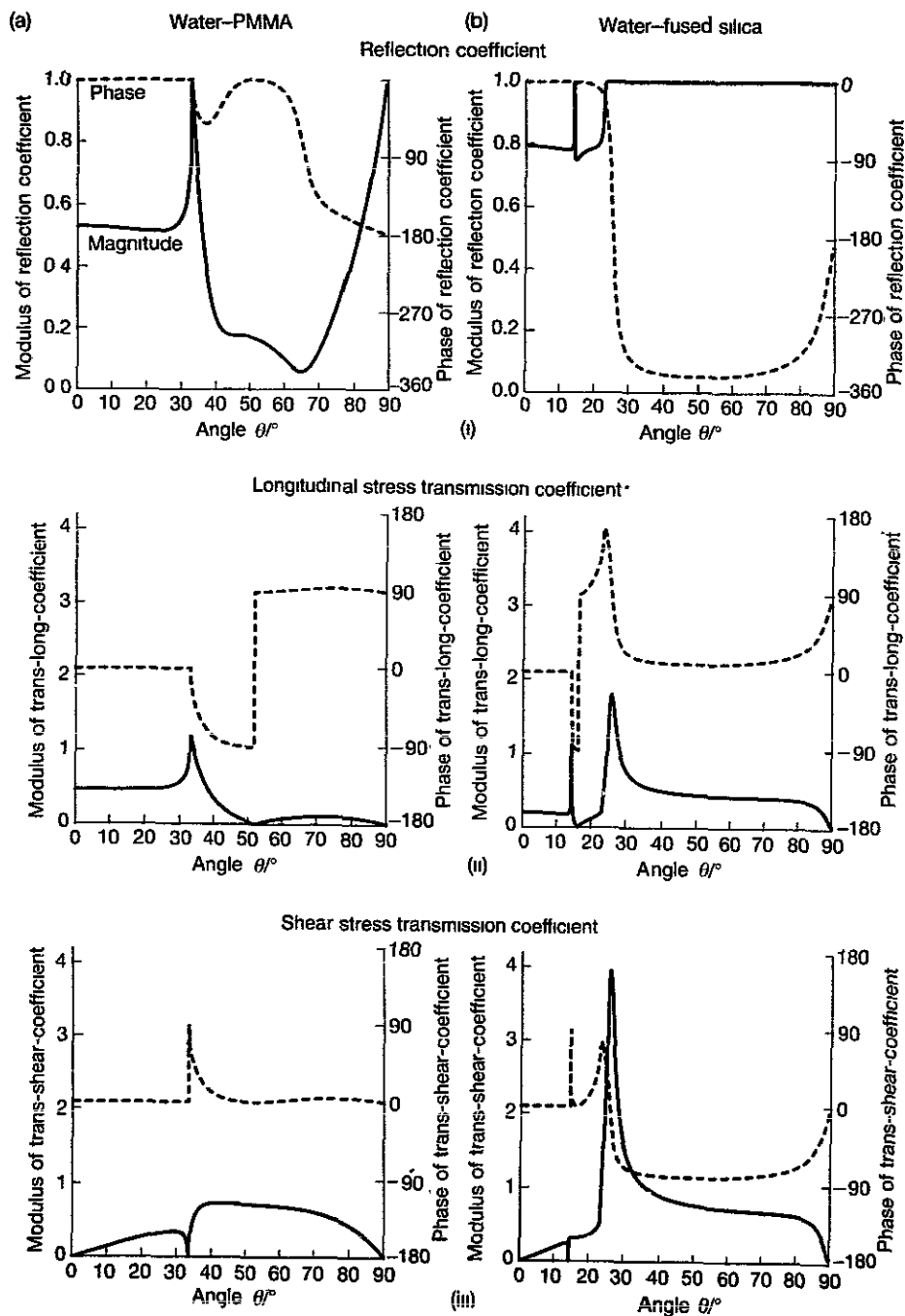


Figure 5. Reflected pressure amplitude and transmitted longitudinal and shear stress amplitudes at a fluid-solid interface: (a) water-PMMA, (b) water-fused silica, (i) reflected wave in the fluid, (ii) transmitted longitudinal wave, (iii) transmitted shear wave, — magnitude (left ordinate), --- phase (right ordinate), equations (2.17)–(2.19).

reached. At this angle  $\sin \theta_1 = 1$  and the reflection coefficient becomes unity, so that all of the incident energy is reflected. The longitudinal transmission coefficient also has a local maximum value; this is not in contradiction with all the energy being reflected, because the longitudinal wave is propagating parallel to the surface and no energy is being carried away from the surface (the transmission coefficients correspond to the stress amplitudes in the material immediately below the surface, and not to the energy flux propagating away from the surface). The shear transmission coefficient is zero at the longitudinal critical angle; at greater angles the shear wave reappears with a  $90^\circ$  phase shift. Further changes occur smoothly up to glancing incidence, at which the reflection coefficient approaches  $-1$  (i.e. unity with a  $180^\circ$  phase shift), and the two transmission coefficients become zero. The phase change of  $180^\circ$  in the longitudinal transmission coefficient at about  $71^\circ$  occurs where the modulus is zero and is equivalent to plotting the modulus as crossing the axis. The shear velocity in PMMA is slower than the velocity in water, and so no shear wave critical angle phenomena occur.

The curve for waves in water incident on fused silica, plotted in figure 5(b), show something extra. The behaviour at the longitudinal critical angle ( $\sim 14^\circ$ ) is qualitatively similar to PMMA. The reflection coefficient is unity, the longitudinal transmission coefficient shows a maximum, and the shear transmission coefficient becomes zero. Beyond this angle no longitudinal waves that carry energy away from the surface are excited in the solid, but shear waves are still excited up to the shear critical angle, beyond which the reflectance is unity. But this does not mean that nothing is happening in the solid, as can be seen by looking at the phase. At normal incidence the phase is zero. At the longitudinal angle there is a slight wiggle but the greatest phase change occurs beyond the shear critical angle. Beyond that angle there can be no excitation of longitudinal or shear waves that propagate energy away from the surface, but there can be excitation of waves that decay exponentially into the bulk. These are just the kind of waves that formed the Rayleigh wave discussed above, and they lead to a phase change of nearly  $2\pi$  that can be seen in the reflectance function just beyond the shear critical angle. When a Rayleigh wave is excited in a solid surface that is in contact with a fluid, it is a leaky Rayleigh wave, because it can reradiate, or leak, energy back into the fluid in the form of waves. The angle at which this occurs is called the Rayleigh angle, and in the limit of very light loading it would be the angle at which the tangential component of the wavevector in the fluid matches the propagation vector of the Rayleigh wave. Because the Rayleigh wave is leaking energy into the fluid, its wavevector is complex, with the imaginary part describing the exponential attenuation due to the leaking. This has the effect of broadening the range of angle over which waves in the fluid can couple to leaky Rayleigh waves in the solid. But the value of  $k_v$  at which the phase of the reflectance function is  $-\pi$  is independent of the properties of the coupling fluid. This can be seen when the reflectance function is expressed in the form of (2.21). The phase change of  $-\pi$  occurs when  $Z_{\text{tot}} = 0$ , and by inspection  $Z_{\text{tot}}$  is a function only of the properties of the solid.

#### 2.4. Contrast theory: $V(z)$

Any experience with an acoustic microscope quickly reveals that the contrast varies sensitively with the distance between the lens and the surface of the specimen. The signal is greatest when the specimen surface is at the focus of the lens. As the specimen is moved from the focal position towards the lens the contrast in an image varies, and in some cases there can even be reversal of the relative contrast from different parts



of an image. If the lens is kept over a single point on the specimen and moved towards the specimen from the focal position, the signal can undergo a series of oscillations [Weglein and Wilson 1978]. This behaviour is best visualized as a  $V(z)$  curve. Here  $V$  refers to the video or envelope-detected signal that is used to modulate the brightness of the picture, and  $z$  refers to the amount by which the specimen surface is displaced from the focal plane of the lens. By convention the focal position is designated  $z = 0$ , and displacement of the specimen towards from the lens is taken as negative. The process of decreasing the separation of the lens and specimen relative to the focal distance is often referred to as defocusing: the most interesting contrast from solids usually occurs at negative defocus.

A picture of the waves that have been excited in a large-scale model, revealed by stroboscopic Schlieren photography, is given in figure 6 (Negishi and Ri 1987). The

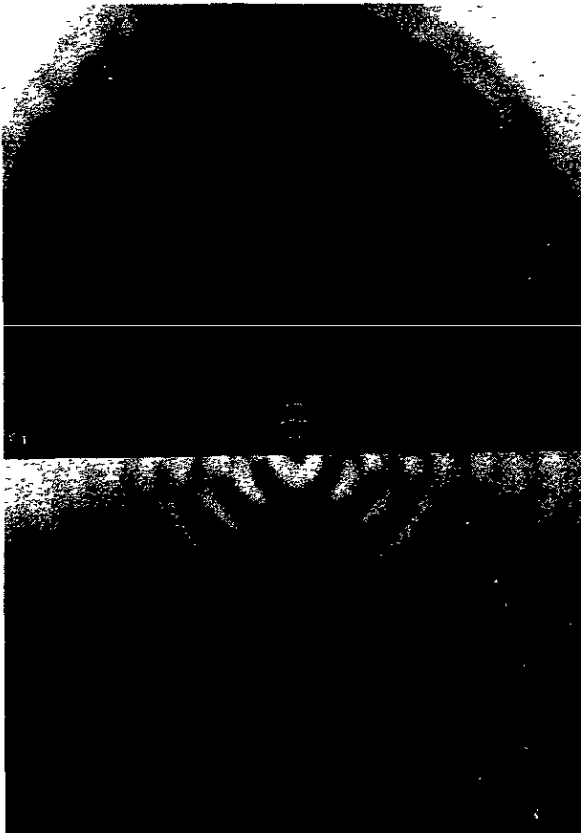


**Figure 6.** Reflection and transmission of acoustic waves focused on a glass surface, visualized by stroboscopic photoelasticity with a Schlieren optical system. The coupling fluid is water, and the lens and specimen are made of optical glass (BK-7). The frequency of the acoustic pulse is 1.2 MHz, and the radius and focal length of the lens are 20 and 27 mm. The longitudinal and shear acoustic velocities in the glass are  $v_l = 6000 \text{ m s}^{-1}$  and  $v_s = 3670 \text{ m s}^{-1}$ , giving Rayleigh velocity  $v_R \approx 0.912v_s \approx 3350 \text{ m s}^{-1}$  and Rayleigh angle  $\theta_R \approx 26^\circ$  (Negishi and Ri 1987).

lens and the specimen were made of glass, and the coupling fluid was water. The tail end of the acoustic pulse has reached the surface of the specimen, and all of the pulse ahead of that has either propagated into the specimen or been reflected from its surface. In the specimen, the shear wave is propagating radially from the focus on the surface of the specimen; the greatest amplitude of the shear wave occurs around  $40^\circ$ . The shear wave vanishes in the normal direction, and the longitudinal wave is not revealed by the imaging conditions used. Close to the surface another wave is present in the solid; this is the Rayleigh wave. There is a weak null between the shear wave and the Rayleigh wave, and careful counting of wavefronts reveals that about 6.5 Rayleigh wavelengths correspond to six shear wavelengths, indicating that the Rayleigh velocity is about 92% of the shear velocity. As the Rayleigh waves propagate away from the focus, they generate plane waves in the water whose wavefronts propagate along a direction corresponding to the Rayleigh angle  $\theta_R$ . The amplitude of the Rayleigh waves decays due to coupling into the water by  $1/e$  over a distance of about 5 Rayleigh wavelengths. Within the arc subtended on each side by the Rayleigh angles from the focus, a cylindrical wave is present, corresponding to the geometrical reflection. At the join between this and the plane waves excited by Rayleigh waves in the solid there is a mismatch of half a wavelength, corresponding to the phase change of  $\pi$  associated with Rayleigh reflection, together with a slight increase in amplitude at this end of the Rayleigh-excited waves (Tew *et al* 1988). The confusion of waves inside the lens indicates some of the reverberations that may occur in practice, giving rise to oscillations of periodicity half the water wavelength in the variation of the signal with defocus. In high-stiffness specimens the Rayleigh wave activity captured so beautifully in this figure plays a central role in the contrast.

**2.4.1. Ray model of  $V(z)$ .** The rays in a microscope with a specimen in which Rayleigh waves can be excited, and which is defocused towards the lens, are sketched in figure 7. Most rays from the lens are reflected specularly from the specimen, and then pass through the lens with an inappropriate angle to contribute significantly to the excitation of the transducer (ray  $aa'$ ). However, the ray ( $bb'$ ) that propagates along the axis of

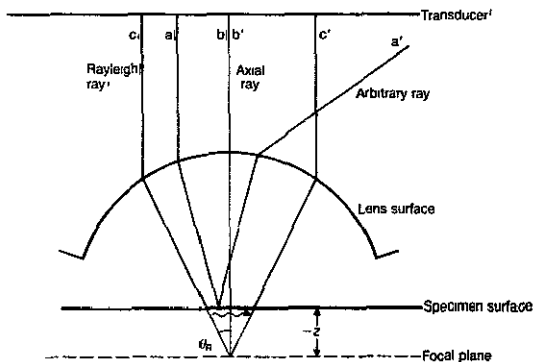


**Figure 7.** Ray model of an acoustic lens with negative defocus:  $aa'$  is an arbitrary ray, which is reflected at such an angle that it misses the transducer (or else hits the transducer obliquely and therefore contributes little to the signal because of phase cancellation across the wavefront);  $bb'$  is the axial ray, which goes straight down and returns along the same path,  $cc'$  is the symmetrical Rayleigh propagated wave, which returns to the transducer normally and so also contributes to the signal.

the lens (normal to the specimen surface) propagates back along the same path after reflection. And the ray ( $cc'$ ) that is incident on the specimen at the Rayleigh angle,  $\theta_R \equiv \sin^{-1}(v_0/v_R)$ , excites a Rayleigh wave in the surface of the specimen which in turn excites waves in the fluid at the Rayleigh angle. The important ray is the one that propagates back to the lens along a path symmetrical to the initial ray that excited the Rayleigh wave. Both the axial ray and this Rayleigh wave contribute to the signal at the transducer. Although they are incident at different places on the transducer, the piezoelectric voltages that they excite are summed with respect both to amplitude and to phase, so that their complex-valued sum is detected, and therefore interference effects between them are observed (Weglein 1979, Parmon and Bertoni 1979).

As  $z$  changes, the phases of these two rays change at different rates, so that they will alternate between constructive and destructive interference. The phase  $\phi_G$  of the geometrically reflected normal ray is

$$\phi_G = -2k_0 z \quad (2.27)$$

where  $k_0$  is the wavenumber in the fluid. The phase  $\phi_R$  of the Rayleigh ray advances by virtue of the shortening of the path in the fluid, but is delayed by the path as a Rayleigh wave in the specimen surface. The overall phase is

$$\phi_R = -2k_0 z \left( \frac{1 - \sin^2 \theta_R}{\cos \theta_R} \right) - \pi \quad z < 0 \quad (2.28)$$

since by Snell's law  $k_R = k_0 \sin \theta_R$  (2.14). The extra term  $\pi$  is associated with the phase change of  $\pi$  in the reflection coefficient at the Rayleigh angle in figure 5(b)i. The phase of the Rayleigh ray can be further simplified using trigonometrical identities. If the output of the transducer is detected by a phase-insensitive circuit (as is usually the case), then it is the difference between the phase of the two rays that is important. This is

$$\phi_G - \phi_R = -2k_0 z (1 - \cos \theta_R) + \pi. \quad (2.29)$$

As the specimen is moved towards the lens, the two rays alternate between being in phase and out of phase. The period  $\Delta z$  of the resulting oscillations in  $V(z)$  is the movement in the  $z$ -direction needed for a change of  $2\pi$  in the relative phase. In terms of the wavelength in water, this is

$$\Delta z = \frac{\lambda_0}{2(1 - \cos \theta_R)} \quad (2.30)$$

with  $\theta_R$  given by Snell's law,

$$\sin \theta_R = \frac{v_0}{v_R} \quad (2.31)$$

where  $v_0$  is the wave velocity in the fluid, and  $v_R$  is the velocity of the Rayleigh wave in the surface of the specimen. The expression for the periodicity of the oscillations in  $V(z)$  is of fundamental importance, and must be understood by every acoustic microscopist.

A derivation analogous to that of (2.29) gives the change in the total attenuation suffered by the Rayleigh ray,

$$\Delta \alpha = 2z(\alpha_0 \sec \theta_R - \alpha_R \tan \theta_R). \quad z < 0 \quad (2.32)$$

The amplitude of the Rayleigh ray will vary as  $\exp[-2z(\alpha_0 \sec \theta_R - \alpha_R \tan \theta_R)]$ . If the Rayleigh contribution to  $V(z)$  is smaller than the geometrical contribution, the amplitude of the oscillations in  $V(z)$  will follow the same exponential decay.

Although this ray derivation is so simple, it gives an extremely useful intuitive picture of what is going on. A more detailed ray model starts by separating the two components of reflection in the way described by (2.23), and treating the amplitude of the rays in the lens and at the transducer quantitatively (Bertoni 1984). Let  $D$  be the distance between the transducer and the lens surface;  $q$ , the focal length of the lens (both of these being measured from the lens surface at the axis);  $n$ , the refractive index of the lens (the ratio of the velocity in the coupling fluid to the longitudinal velocity in the lens material);  $\lambda_0$ , the wavelength in the coupling fluid, and  $\alpha_0$ , the attenuation in the coupling fluid. For negative defocus beyond about  $z \ll -\lambda_0$ , the geometrical contribution to the signal is

$$V_G(z) \approx V_0 A R_0(0) \left( \frac{-2z_0}{\pi z} \right) \sin X_R \exp[2(ik_0 - \alpha_0)z + iX_R]$$

where

$$A = -\exp[i2k_0(Dn + 1) - 2\alpha_0 q]$$

and

$$X_R = \frac{\pi}{2} \frac{z}{z - z_0} \quad z \ll -\lambda_0. \quad (2.33)$$

The approximations are valid when the distance from the transducer to the back focal plane of the lens is close to the Fresnel distance of the transducer ( $\lambda_0/a_T^2$ , where  $a_T$  is the radius of the transducer), as it is in most high-resolution lenses. The Rayleigh reflection at the surface of the specimen leads to a family of rays at the Rayleigh angle propagating towards the lens. Because in any plane through the axis they are parallel, they are brought to a focus at the back focal plane of the lens, and if there is axial symmetry they will be focused in a ring, of radius  $a_R \approx q \sin \theta_R$ . For  $z \ll -\lambda_0/(4 \cos \theta_R \sin^2 \theta_R)$  the situation can be described by considering the incident ray at the Rayleigh angle as exciting a leaky Rayleigh wave in the specimen, which in turn excites rays at the Rayleigh angle in the liquid. The Rayleigh contribution to the signal at the transducer is then

$$V_R(z) \approx V_0 A 2\pi^{1/4} \left( \frac{q}{a_T} \right)^{3/2} \frac{\rho_0}{\rho_1} \sin^{5/2} \theta_R e^{i\pi} \exp(i2k_0 z \cos \theta_R) \exp[2z(\alpha_T \tan \theta_R - \alpha_0 \sec \theta_R)] \quad z \ll -\lambda_0/(4 \cos \theta_R \sin^2 \theta_R). \quad (2.34)$$

The dependence of  $V_R$  on  $z$  is rather simple. The phase variation is given by the second exponential term, the first describing the constant phase change of  $-\pi$  associated with the phase change in the reflectance function at the Rayleigh angle. The final exponential term describes the change in attenuation due to the decrease in water path and increase in Rayleigh wave path as the defocus increases. Both the geometrical contribution and the Rayleigh contribution can thus be expressed in terms of material constants and the geometry of the lens, and therefore be directly compared. The complex summation of (2.33) and (2.34) enables  $V(z)$  to be computed, and leads immediately to oscillations with periodicity

$$\Delta z = \frac{2\pi}{2k_0 - 2k_0 \cos \theta_R} = \frac{\lambda_0}{2(1 - \cos \theta_R)} \quad (2.35)$$

as before. The decay of  $V_R(z)$  in (2.34) has the same form as in (2.32), and once again if  $V_R(z) < V_G(z)$  the oscillations in  $V(z)$  will have an identical decay.

The ray model can be extended to give an account of the contrast in specimens in which lateral longitudinal waves play a role (Chan and Bertoni 1990). The results for Rayleigh waves can be adapted for lateral longitudinal waves by substituting  $k_0 \rightarrow k_1$ ,  $\theta_R \rightarrow \theta_1$ , and multiplying by the factor

$$M = \frac{B(k_1)}{2\alpha_R} \frac{1}{\sqrt{2\pi k_1}} \frac{e^{i\pi/4}}{|x-x'|^{3/2}} \quad (2.36)$$

where  $B(k_1)$  is taken from (2.26). Since  $k_1$  is a real number, whereas  $k_p$  is complex, the exponential decay of the Rayleigh wave goes out, to be replaced by the algebraic decay in amplitude of  $\frac{3}{2}$  power. Any remaining attenuation,  $\alpha_1$ , is due to damping or scattering in the solid. With these substitutions, the contribution to the response in the microscope due to lateral longitudinal waves is, by analogy with (2.34),

$$V_1 = V_0 AB(k_1) \frac{1}{k_0} \left( \frac{(\sqrt{\pi} \lambda_0 f^3)^{1/2}}{(2|z| \tan \theta_1)^{3/2} (\lambda_0 D/n)^{3/4}} \right) e^{i5\pi/4} \exp(i2k_0 z \cos \theta_1) \quad (2.37)$$

$$\times \exp[2(\alpha_1 \sin \theta_1 - \alpha_0) z \sec \theta_1] \quad z \ll -\frac{2}{\pi} \left( \frac{c_{11}}{c_{12}} \right)^4 \left( \frac{\rho_0}{\rho_1} \right)^2 \frac{\lambda_0}{\cos \theta_1}.$$

The defocus beyond which this is valid is  $z \ll -3\lambda_0$  for PMMA,  $z \ll -\lambda_0$  for aluminium, but  $z \ll -77\lambda_0$  for fused silica. Lateral rays make an important contribution to  $V(z)$  for polymers in which  $v_1 \geq v_0/\sin \theta_0$  (where  $\theta_0$  is the lens angle) and in which Rayleigh waves are not excited. An example is PMMA, whose reflectance function is plotted in figure 5(a)i. In faster materials, lateral longitudinal waves with their algebraic decay are still significant at larger values of  $-z$ , after the Rayleigh waves with their punishing exponential decay have become insignificant. Lateral waves give rise to oscillations in  $V(z)$  described by the same relationship as (2.30) and (2.35), but with the longitudinal critical angle. The periodicity is therefore

$$\Delta z_1 = \frac{\lambda_0}{2(1 - \cos \theta_1)}. \quad (2.38)$$

**2.4.2. Plane wave model of  $V(z)$ .** A simplified picture of the transducer, lens surface and reflecting object is shown in figure 8. The waves radiated by the transducer are refracted by the lens so as to form a spherical wavefront centred on the focal point of the lens. Each point on this wavefront can be described by its angular coordinates from the focus; let these be  $\theta$  for the zenithal angle (i.e. the angle to the lens axis, taken to be normal to the specimen surface), and  $\phi$  for the azimuthal angle. Thus the spherical wave emerging from the lens can be described by a function  $L_1(\theta, \phi)$ . The wave is reflected from the specimen surface with a reflectance function  $R(\theta, \phi)$ , which also depends on these angles. Finally, the wave returns through the lens to the transducer, where it is detected with a sensitivity  $L_2(\theta, \phi)$ . The total received signal can therefore be calculated by integrating over  $\theta$  and  $\phi$ :

$$V = \int_0^{\pi/2} \int_{-\pi}^{\pi} L_1(\theta, \phi) R(\theta, \phi) L_2(\theta, \phi) \sin \theta \, d\phi \, d\theta. \quad (2.39)$$

Since  $L_1(\theta, \phi)$  and  $L_2(\theta, \phi)$  depend only on the geometry and materials of the lens, it is convenient to combine them in a single pupil function, which may be defined as

$$P(\theta, \phi) = L_1(\theta, \phi) L_2(\theta, \phi) / \cos \theta. \quad (2.40)$$

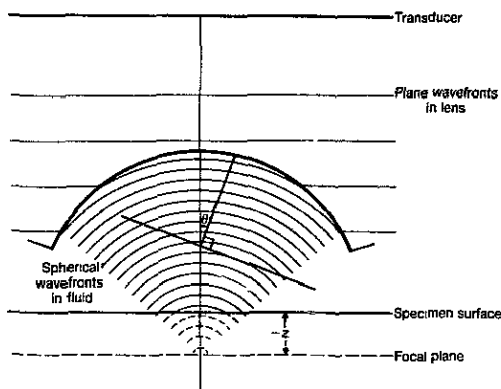


Figure 8. Wave model of an acoustic lens focussed on a surface; the tangent to one of the wavefronts illustrates one of the family of plane waves of which the wavefront is considered to be composed

The  $\cos \theta$  term in the definition allows for the obliqueness of the excitation of the spherical waves by plane waves incident on the refracting surface. It is analogous to the reduction in the amount of sunlight per unit area falling on the earth at high angles, and means that a lens with uniform illumination and perfect transmission up to a given cut-off angle would have a pupil function of unity up to that angle and zero above it. With this definition of the pupil function, the response is

$$V = \int_0^{\pi/2} \int_{-\pi}^{\pi} P(\theta, \phi) R(\theta, \phi) \sin \theta \cos \theta \, d\phi \, d\theta. \quad (2.41)$$

Most imaging lenses are designed to have axial symmetry, so that  $P$  is independent of  $\phi$ . If the specimen is isotropic then the  $\phi$ -integration may be absorbed in  $P$ , so that the expression for  $V$  simplifies to

$$V = \int_0^{\pi/2} P(\theta) R(\theta) \sin \theta \cos \theta \, d\theta. \quad (2.42)$$

This expression describes the response of the system to a specimen at focus. If there are no aberrations, then at focus the phase of all the plane wave contributions at different angles is the same. But the functions in the integrand can be complex valued.  $R(\theta)$  has both amplitude and phase, and this can be represented by making it complex, with the angle in the complex plane representing the phase. Similarly, any lens aberrations can be described by making  $P(\theta)$  complex, though usually phase aberrations can be very small even for acoustic lenses of large opening angle.

If the specimen is moved away from the focal position, then this will cause a phase shift that depends on  $\theta$ . If the wavenumber in the coupling fluid is  $k = 2\pi/\lambda_0$ , then the  $z$ -component of the wavevector is  $k_z = k \cos \theta$ . Defocusing the specimen by an amount  $z$  causes a phase delay of  $2z k_z$ , or  $2z k \cos \theta$  (the factor of two arises because both the incident wave and the reflected wave suffer a change in path length). Expressing this phase delay as the complex exponential of a phase angle, the response of the microscope with a defocus  $z$  is

$$V(z) = \int_0^{\pi/2} P(\theta) R(\theta) e^{i2kz \cos \theta} \sin \theta \cos \theta \, d\theta. \quad (2.43)$$

This is the basic expression for the response of the microscope to a uniform isotropic specimen at a defocus  $z$  [Wickramasinghe 1978, 1979; Atalar 1978, 1979; Quate *et al* 1979; Sheppard and Wilson 1981; Liang *et al* 1985].

The equation for  $V(z)$  can be expressed as a Fourier transform by a suitable change of variables [Hildebrand *et al* 1983; Ilett *et al* 1984; Liang *et al* 1985; Fright *et al* 1989]. The new variables are defined:

$$\begin{aligned} u &= kz \\ t &= \frac{1}{\pi} \cos \theta. \end{aligned} \quad (2.44)$$

Then (2.43) may be written as

$$V(u) = \int_0^{1/\pi} P(t)R(t) e^{i2\pi ut} t \, dt. \quad (2.45)$$

With the further substitution

$$Q(t) = P(t)R(t)t \quad (2.46)$$

$V(u)$  may be written as

$$V(u) = \int_0^{1/\pi} Q(t) e^{i2\pi ut} dt. \quad (2.47)$$

Equation (2.47) describes a Fourier transform [Bracewell 1978], with  $V(u)$  and  $Q(t)$  as the transform pair. The limits of the integration should be from  $-\infty$  to  $+\infty$ , but since  $Q(t)$  vanishes outside the given limits this makes no difference.

There are two particular discontinuities in  $R(t)$  that are of great importance for materials in which Rayleigh waves are excited. The first occurs at  $t_0 = 1/\pi$ , because beyond that value  $Q(t)$  changes discontinuously to zero. The second is at  $t_R = \cos \theta_R / \pi$ , because around the Rayleigh angle  $\theta_R$  there is a phase change of  $2\pi$  in  $R(\theta)$ , cf. figure 5(b)i, and hence in  $Q(t)$ . The Fourier relationship gives oscillations in  $V(u)$  of periodicity

$$\Delta u = \frac{1}{t_0 - t_R}. \quad (2.48)$$

In terms of the original variables the period of the oscillations in  $V(z)$  is

$$\Delta z = \frac{\lambda_0}{2(1 - \cos \theta_R)} \quad (2.49)$$

which is identical to (2.30).

**2.4.3. Tweedledum or Tweedledee?** The Fourier theory and the ray model offer quite different insights into imaging theory. Both enable  $V(z)$  to be calculated *ab initio*. Figure 9 shows  $V(z)$  curves calculated from field theory and from ray theory, compared with a measured curve. In the Fourier model it is not necessary to know about Rayleigh waves or any other surface wave modes, because these are all contained implicitly in the reflectance function. Thus in any situation in which the reflectance function of a surface can be calculated (even for a complicated layered structure), and for which the pupil function of the lens is known, the complete  $V(z)$  curve can immediately be computed without any approximations. In practice, accurate measurement of the pupil function can be very difficult, but since it is constant for a given lens at a given frequency

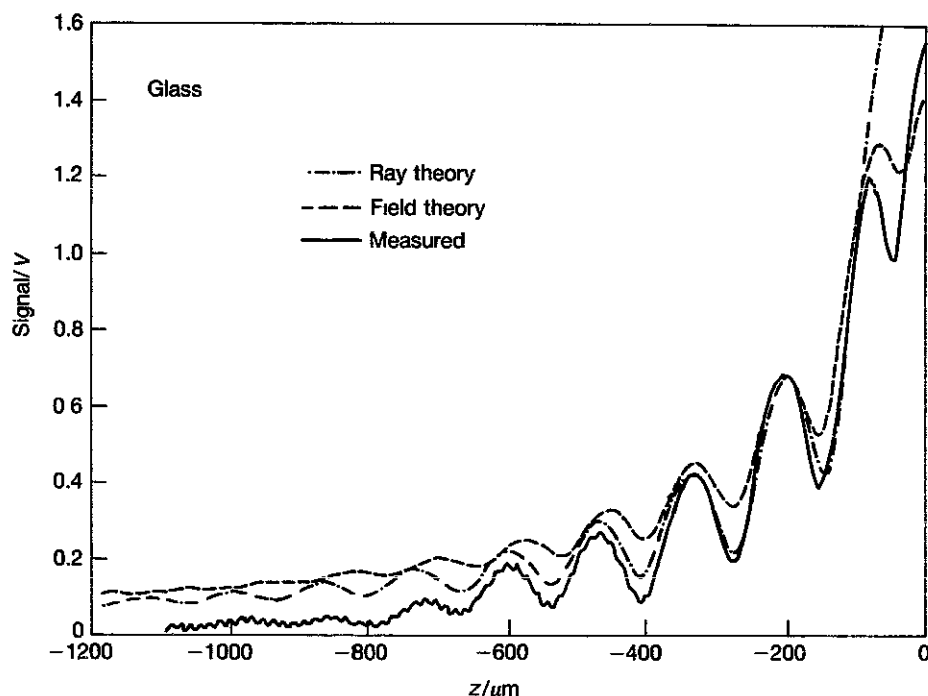


Figure 9. Calculated and measured  $V(z)$  curves for a glass microscope slide: --- field theory; - · - ray theory; — measured. The lens was of fused quartz, with focal length  $q = 4$  mm, aperture radius  $a_0 = 2.5$  mm (giving  $NA = 0.625$ ), and length from transducer to lens surface  $D = 60$  mm, the frequency was  $f = 49$  MHz. The field theory calculations were made by computing the field in the back focal plane of the lens due to the transducer, truncating the field at the lens aperture and multiplying by the two-way transmission coefficient at the lens-water interface, and then performing the integration in (7.14), the ray theory calculations were made using the equations in section 7.2.2 (Chiznik 1991).

it is at least possible to make comparisons between  $V(z)$  curves for different specimen parameters. Simple calculations of  $R(\theta)$  and hence  $V(z)$  from (2.17) and (2.43) can give a great deal of insight into how the contrast can be expected to vary as a function of defocus and specimen parameters.

The ray model requires many more assumptions about the contrast mechanism. It assumes that the fluid loading is light, so that the fluid causes only a small perturbation to the Rayleigh wave propagation. And any other interactions with the fluid, such as lateral wave excitation, are left out unless they are explicitly included. But when Rayleigh waves do dominate the contrast, as is the case with many materials, then the ray model gives a very useful account of what is going on, and one that is so simple that it is possible to visualize the Rayleigh waves in a way that soon becomes intuitive. In a sense the very weakness of the ray model is its strength: by restricting itself to the Rayleigh wave and the normal wave it emphasizes those very waves that in the cases where it is applicable do all the work.

If the first role of imaging theory is to enable the microscopist to understand the images that he sees, the second role is to show how to interpret the contrast quantitatively. By expressing the reflectance function in terms of the inverse Fourier transform



of  $V(z)$ , it is in principle possible to use the Fourier theory to deduce the reflectance function from a measured  $V(z)$  curve. But then the strength of the Fourier theory is its weakness. Precisely because it gives you everything, the Fourier theory is not selective. If, as is often the case, the interaction with the specimen is concentrated around the Rayleigh angle, then a ray theory that explicitly makes that assumption will, for that very reason, select the information that is most reliable. This will influence the choice of method for quantitative measurements in acoustic microscopy.

### 3. Some pictures

#### 3.1. A variety of features

A section through a glass matrix composite is shown in figure 10. The matrix is a borosilicate glass, whose composition can be tailored for optimum compatibility with the fibres, and its relatively low viscosity at high temperature enables almost complete penetration of the matrix into the fibre bundles during fabrication. The fibres are composed mainly of silicon carbide; their commercial name is Nicalon. The composite has a flexural strength of 1.25 GPa and a fracture toughness of  $70 \text{ MN m}^{-3/2}$ . Figure 10(a) is an acoustic picture, at 1.9 GHz: an optical picture of another area of the specimen is shown in figure 10(b). Newcomers to acoustic microscopy find optical comparisons reassuring, though as confidence is gained such comparisons become less and less necessary. Crucial questions for the development of a composite like this one are: are its properties, such as its strength and toughness at high temperatures, the best that can be obtained? If so, how do you make sure that those properties are consistently achieved? If not, how do you improve them still further?

Figure 10(a) shows a wealth of detail. First, and most obvious, the fibres have a different contrast from the matrix. In the imaging conditions here, the fibres are darker than the matrix. By simply counting the fibres and measuring their diameters, the mean SiC fibre diameter is  $16 \mu\text{m}$ , and the area fraction is 0.49. But the matrix appears to be composed of two phases. About 70% of the matrix area appears homogeneous, while the remaining 30% appears granular, with a grain size less than  $10 \mu\text{m}$ . The bright, homogeneous region is borosilicate glass, behaving itself perfectly well. The crystalline phase was subsequently confirmed, using both energy dispersive and wavelength dispersive spectroscopy on an electron microprobe and also x-ray diffraction, to be cristobalite. Cristobalite is an allotrope of silica with a cubic crystal structure, which is stable at high temperatures ( $1470$ – $1713^\circ\text{C}$ ) under atmospheric pressure. The precipitation of cristobalite, known as devitrification, is likely to occur when borosilicate glass is held for a prolonged time between the glass softening temperature and the crystallization temperature. The fabrication procedure for the 7740/SiC composite involves just such conditions. The cristobalite seems to grow to form a layer  $3$ – $5 \mu\text{m}$  thick around the fibre, but it seems to nucleate away from the fibre too.

There is a phenomenon in the acoustic picture that is not seen by any other kind of microscopy. In the acoustic micrograph there are fringes, both in the glass and in the silicon carbide. In the silicon carbide they are more widely spaced than in the glass, and they could be mistaken for growth rings, perhaps associated with the processing of the fibres, such as are found in a tree trunk. But they are not growth rings, they are an interference effect associated with acoustic waves excited in the

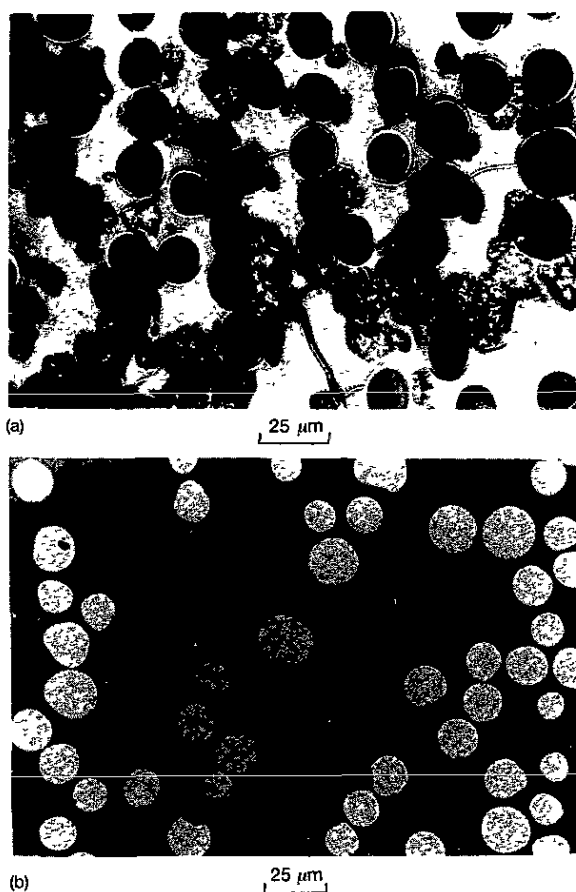


**Figure 10.** A section through a glass matrix composite (a) acoustic micrograph, 1.9 GHz,  $z = -2.8 \mu\text{m}$ , (b) optical micrograph. The matrix is borosilicate glass, Corning code 7740, composition by weight,  $\text{SiO}_2$  81%,  $\text{Al}_2\text{O}_3$  2%,  $\text{B}_2\text{O}_3$  13%. The fibres are silicon carbide, manufactured by Nippon Carbon under the name Nicalon (Yajima *et al* 1978) nominal diameter,  $15 \mu\text{m}$ , tensile strength, 2.75 GPa; Young modulus, 196 GPa, Poisson ratio, 0.15, density,  $2.55 \text{ Mg m}^{-3}$ . The composite has fibre volume fraction 0.49, flexural strength, 1.25 GPa; Young modulus, 120 GPa, work of fracture  $40 \text{ kJ m}^{-2}$  (Lawrence 1990).

surface. These are the Rayleigh waves introduced in section 2.2, whose longitudinal and shear components decay exponentially away from the surface. In acoustic microscopy, surface waves can be excited rather strongly in a solid, and interference with specularly reflected waves gives rise to the interference fringes observed. The spacing of the interference fringes is half the Rayleigh wavelength. The Rayleigh wavelength in the fibres must be greater than it is in the matrix, because the separation of the fringes is smaller in the matrix than it is in the fibres. In the matrix the fringes are associated with at least three kinds of features. First, there are fringes around the fibres that are loci of constant distance from the interface between the fibre and the matrix, just as the fringes inside the fibres are. Then there are fringes, too, that seem to run around areas of cristobalite, or perhaps at constant distance from interfaces between

crystalalite and glass. Finally, there are fringes that seem to run alongside cracks in the glass. The acoustic microscope has a greatly enhanced sensitivity to cracks or boundaries that run up to the surface, and is able to give strong contrast from them even when they are much finer than the wavelength being used for imaging. This sensitivity is associated with the excitation of Rayleigh waves in the surface, and their scattering by cracks or by the change of impedance as they pass from one material to another.

A pair of pictures of an area of a polished  $30\text{ }\mu\text{m}$  thick specimen of granodiorite, a type of granitic rock, is shown in figure 11 (Rodríguez-Rey *et al* 1990). This specimen

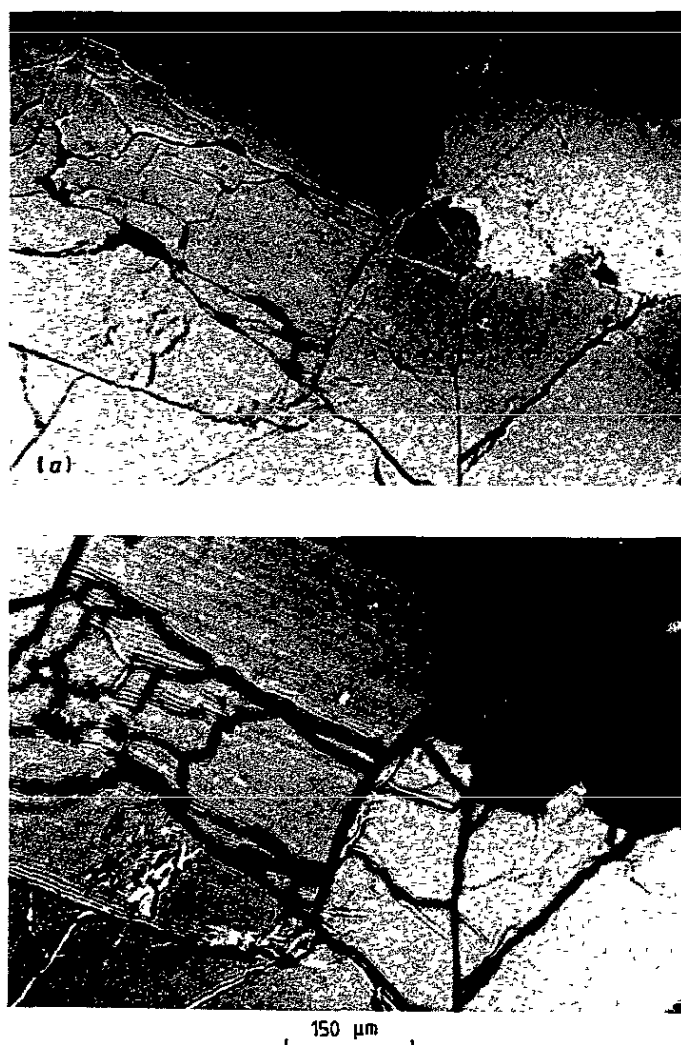


**Figure 11.** Polished granodiorite section containing plagioclase, biotite, and quartz; 400 MHz (a)  $z = -5\text{ }\mu\text{m}$ , (b)  $z = -25\text{ }\mu\text{m}$  (Rodríguez-Rey *et al* 1990).

was taken from the quarries used in the sixteenth century to provide building stones for the monastery of San Lorenzo el Real de El Escorial, near Madrid in Spain. Great care was taken in the preparation of the specimen to obtain a flat surface with no relief polishing, using standard petrographic techniques (except that only one surface is needed for acoustic microscopy in reflection). Three different minerals are present in this area of the specimen. In the top right corner is biotite, a highly anisotropic phyllosilicate. In the top left region is plagioclase, which appears in the rock as zoned crystals ranging in composition from oligoclase to andesine. Finally, the mineral in the lower region of the picture is quartz.

The difference between the pictures is due to the different distance from the lens at which each was taken. No-one can operate an acoustic microscope for very long without discovering that the contrast can vary dramatically as you move the specimen up and down relative to the lens. Indeed, it is quite possible for contrast reversals to occur between, for example, one grain in a specimen and another. The contrast of the biotite varies quite markedly between (a) and (b), relative to the plagioclase and the quartz. Plagioclase and quartz give rather similar contrast to each other in both pictures, they are distinguished by the twinning microstructure in the plagioclase. The variation of the signal from any given point on the specimen with the distance between the lens and the specimen is the experimental consequence of the  $V(z)$  theory presented in sections 2.4.1–2.4.3.

The relationship between contrast reversals in pictures and a  $V(z)$  curve is illustrated in figure 12. A model specimen was used, consisting of a polished specimen of human tooth enamel, half of which was then exposed to a demineralizing acid.  $V(z)$  curves were measured over the two regions, and these are plotted in the figure. As usual, negative defocus corresponds to moving the lens closer to the specimen. Three pictures of the specimen are shown, taken at focus and at two negative values of defocus, and these are related in the figure to the points on the  $V(z)$  curves at the same values of  $z$ . In the first picture (a), taken at focus, there is almost no contrast between the two regions of the specimen. Comparison with the  $V(z)$  curves confirms that they have almost the same value at  $z = 0$ , so that no contrast in the picture is to be expected. In

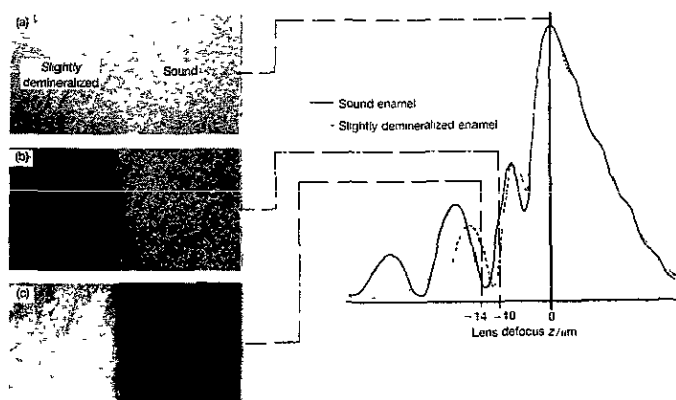


**Figure 12.** Acoustic images and  $V(z)$  curves for a specimen of human tooth enamel prepared with the left half slightly demineralized and the right half sound.  $V(z)$  curves. — sound enamel; --- slightly demineralized. Micrographs (a)  $z = 0$ , (b)  $z = -10 \mu\text{m}$ , (c)  $z = -14 \mu\text{m}$ ; 370 MHz (Peck and Briggs 1987).

the second picture (*b*), taken at  $z = -10 \mu\text{m}$ , the sound enamel is bright relative to the demineralized enamel, and this corresponds to a higher value of the sound enamel  $V(z)$  curve at that value of  $z$ . As  $z$  becomes more negative the curves swap over, until at  $z = -14 \mu\text{m}$  the signal is larger over the demineralized enamel, and so the demineralized enamel is brighter than the sound enamel in the third picture (*c*). An appreciation of this kind of relationship between  $V(z)$  behaviour and the contrast that is seen in pictures is an enormous help in the interpretation of contrast.

The  $V(z)$  curves in figure 12 are purely experimental: indeed, the curves and the pictures are in one sense simply different ways of presenting measurements from the same system. Several points of fundamental importance for practical microscopy follow. First, especially with materials whose elastic properties are significantly different from those of water, very little contrast may be seen at focus. Consciously or unconsciously the operator will find the defocus at which the contrast from the features of interest is optimized. As a starting rule of thumb, this may often occur where the value of  $V(z)$  is about half its maximum. Second, the contrast variations are often at the best where the slope of  $V(z)$  is at its steepest. Third, if the signal is sensitive to  $z$ , then it is also sensitive to topography. Therefore, if contrast from topography is not to swamp contrast from elastic features, the specimen surface must be sufficiently flat that the residual topography causes less than the difference in  $z$  that would correspond to the same signal from elastically different regions of the specimen; in the case of figure 12 this would correspond to variations in surface height considerably less than  $1 \mu\text{m}$ . Fourth, you cannot simply look at an isolated acoustic micrograph and say that bright or dark regions correspond to such-and-such elastic properties, such as high or low stiffness or high or low density. Quantitative (and much qualitative) interpretation of acoustic micrographs depends on knowing how the contrast varies with defocus. Finally, the oscillations at negative defocus in the experimental  $V(z)$  correspond directly to the oscillations in the calculated  $V(z)$ , that were attributed to Rayleigh wave interference. Thus the experimental oscillations confirm that indeed the contrast is being dominated by Rayleigh wave activity, and that to some extent the pictures can be considered as images of factors affecting Rayleigh wave propagation. In some cases, notably in layered and in anisotropic specimens, other kinds of surface waves related to Rayleigh waves also play a role.

### 3.2. Thin films on substrates

The difference between a specimen that is effectively a semi-infinite half-space and one that has a boundary at a finite depth is illustrated in experimental  $V(z)$  curves of two glass specimens in figure 13. The broken curve is  $V(z)$  for a microscope slide 2 mm thick. The solid curve is  $V(z)$  for a glass cover-slip 0.11 mm thick. In a thin plate, such as a cover-slip, Lamb waves can be excited (Auld 1973). At low frequencies the lowest order symmetric mode is like a longitudinal wave, except that because the plate is thin the modulus governing the velocity is  $c_{11} - c_{12}^2/c_{11}$ . If the frequency is increased until the shear wavelength becomes comparable with twice the plate thickness, then the velocity begins to decrease, eventually approaching the Rayleigh velocity. The lowest order antisymmetric mode has a vanishingly small velocity at low frequency, where the motion can be thought of as the plate flapping up and down. As the frequency increases, a small longitudinal component of motion is introduced and at high frequency the velocity also approaches the Rayleigh velocity; indeed, a Rayleigh wave can be considered as a summation in the high-frequency limit of a pair of degenerate symmetric

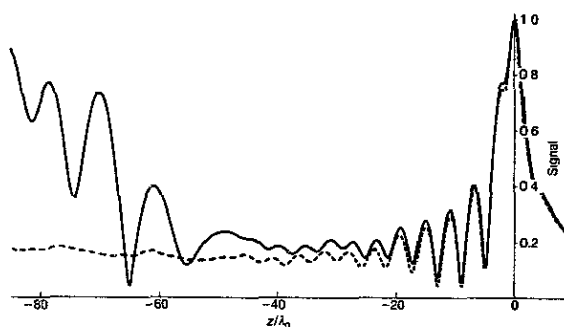


Figure 13.  $V(z)$  curves measured on glass specimens — 0.11 mm thick cover-slip, --- 2 mm thick microscope slide (in this context effectively a semi-infinite half-space solid)

and antisymmetric waves. If  $V(z)$  is measured at a given frequency for a plate whose thickness is less than half the shear wavelength then the two lowest order modes are the ones present;  $V(z)$  contains two oscillations, each with exponential decay, corresponding to these two modes (Kushibiki and Chubachi 1985). If the frequency is increased, more Lamb waves appear. A new symmetric mode appears for each increase in thickness of half a longitudinal wavelength, and a new antisymmetric mode for each half shear wavelength. Each new mode starts with an infinite phase velocity, which decreases towards the shear velocity with increasing plate thickness. When there are more than a very small number of modes present, it becomes unrealistic to try to identify the contributions of each Lamb wave. Perhaps it is best to say simply that Lamb wave modes become important in  $V(z)$  at sufficient defocus, and the values of  $z$  for paraxial focus of shear or longitudinal waves on the lower surface indicate the defocus at which the higher Lamb wave modes begin to be significant. This is analogous to the simple ray argument that in the absence of scattering, Rayleigh waves contribute to  $V(z)$  only at negative defocus.

At small defocus both the curves in figure 13 show oscillations of periodicity  $4.1\lambda_0$ , corresponding to a velocity at  $3100 \text{ m s}^{-1}$ . This is a respectable value for the Rayleigh velocity in crown glass. With a wavelength  $\lambda_0 = 6.6 \mu\text{m}$  and a refractive index  $n = 0.43$  for shear waves, the first paraxial focus on the lower surface of the cover-slip will occur at  $z = -40\lambda_0$ . Beyond this defocus, oscillations develop in the  $V(z)$  curve of the cover-slip with a periodicity of  $9.4\lambda_0$ , indicating a velocity of  $4660 \text{ m s}^{-1}$ . This is too slow to be a lateral longitudinal velocity (and if it were, why are the same oscillations not present in the dashed curve?), so it must relate to a mode that involves shear waves and reflection from the bottom surface of the cover slip. There is no objection to the phase velocity  $\omega/k$ , which is what the  $V(z)$  technique measures, being greater than the velocity of the constituent waves, it is the group velocity  $\partial\omega/\partial k$ , which would be measured by time-resolved techniques, that cannot be greater. For specimens of greater thickness relative to the wavelength than the cover-slip in figure 13, the Lamb modes form almost a continuum, and the concept of focusing on the lower surface becomes more applicable. A similar approach can be applied to a multilayered structure. If it is desired not to image a particular interface, but rather to search for defects at a given depth below a surface, then it may not be necessary to consider Lamb modes at all. Instead, the confocal depth discrimination can be exploited to enhance the strength of the signal from a subsurface scatterer that is in focus. At sufficient depth below the

surface it may be possible also to use a time-resolved technique. But the scope for subsurface focusing (as opposed to Rayleigh wave imaging) in stiff materials becomes severely limited at high frequencies, because of the short working distance imposed by the attenuation in the coupling fluid.

If the specimen has a single surface layer on a substrate, then leaky generalized Lamb waves can be excited (Auld 1973). The character of these waves depends on the ratio of the shear velocities of the layer  $v_{s1}$  and the substrate  $v_{s2}$ . In each case there is a fundamental mode, which in the limit of a very thin surface layer approximates to a Rayleigh wave with a slighted shifted velocity which may be calculated by treating the surface layer as a perturbation. If  $v_{s1} \geq v_{s2}$ , then this is the only wave mode that is bound to the surface, and it exists at all frequencies for which its phase velocity is less than  $v_{s2}$ . In many cases of interest, for example, a polymer coating on a metal substrate, or a metal film on a semiconductor,  $v_{s1} < v_{s2}$ . In this case the perturbed Rayleigh wave is again the lowest order mode, and in general it exists for all thicknesses, becoming a Rayleigh wave in the top coating when the layer becomes much more than a wavelength thick. When the layer is very thin this mode is the only one to be trapped at the surface; as the thickness is increased at a given frequency the next mode to become trapped is the Sezawa wave.

Dispersion relationships of Rayleigh and Sezawa waves for a layer of gold on 42-alloy are plotted in figure 14 (Tsukahara *et al* 1989). The formation of a Sezawa wave can be followed by considering the propagation of an essentially longitudinal wave parallel to the surface with a layer that in the first instance is very thin (Farnell and Adler 1972). The layer perturbs the wave, so that it is slower than the substrate longitudinal wave velocity. Coupling between longitudinal and shear waves can occur only at surfaces and interfaces; if by magic this could be switched off, then the slowed-down longitudinal wave would be trapped at the surface. But because it does couple into shear waves there can be a leakage into bulk shear waves in the substrate. At this stage the wave may be called a pseudo-Sezawa wave. As the layer thickness is increased, the motion in the layer becomes increasingly shear in character, and the velocity of the wave becomes even slower, until at a critical layer thickness it is slower than the substrate shear velocity, at which point the wave becomes a true Sezawa wave because it can no longer leak energy into the substrate. In the limit of a very thick surface layer the Sezawa wave becomes a shear wave in the layer (in certain special combinations of material parameters with  $v_{s1} \approx v_{s2}$  it becomes instead a Stoneley wave trapped at the interface between the layer and the substrate). Both true Sezawa waves

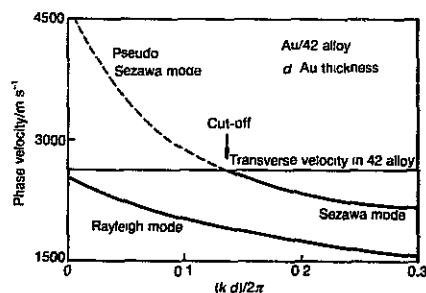


Figure 14. Dispersion relationships for surface waves excited in a half space of 42%Ni-Fe alloy with a layer of gold of thickness  $d$ , and with water loading;  $k = v/\omega$  is the propagation number along the specimen surface (Tsukahara *et al* 1989).

and pseudo-Sezawa waves can couple strongly to waves in a fluid, and therefore cause changes in the phase of the reflectance function. In addition, the pseudo-Sezawa wave causes a dip in the magnitude of the reflectance function because it serves as an effective means of coupling energy to shear waves in the substrate. If the film is lossy (as a polymer coating might well be), then the Sezawa wave can also cause a dip in the reflectance function: in ray terms this corresponds to a ray propagating along the surface, rather like the Rayleigh ray in figure 7, and dissipating energy in the film as it goes.

The dispersive reflectance function for a layer of gold on 42-alloy is shown in figure 15 (Tsukahara *et al* 1989). The reflection coefficient ( $a$ ) has been plotted upside down in order to display high coupling into the substrate as peaks in  $1 - |R(\theta)|$ . At zero normalized thickness  $R(\theta)$  has the familiar form of a fluid-loaded half-space. As the thickness is increased so the pseudo-Sezawa wave can be seen to develop, with decreasing velocity (given by Snell's law as  $v_0/\sin \theta$ ), until the critical angle for shear waves in the substrate, when it becomes a true Sezawa wave and ceases to couple any energy into the substrate, manifesting itself only in the phase of  $R(\theta)$ . Higher modes can also be seen beginning to develop at greater layer thicknesses. Just as in a uniform half-space the interaction between waves in the fluid and the solid does not stop at the shear critical angle, but is manifested in a phase change of  $2\pi$ , so also there is a phase change associated with Sezawa waves. In the plot of the phase of the dispersive reflectance function ( $b$ ), the  $2\pi$  phase change is well pronounced, especially in the region where the reflectance function is unity. The analogy with Rayleigh waves is a close one; the  $2\pi$  phase change is associated with the excitation of Sezawa waves which cannot radiate energy into the solid but can couple weakly into waves in the fluid. Pseudo-Sezawa waves have been observed in  $V(z)$  data in acoustic microscopy (Tsukahara *et al* 1984), and they have also been identified in a reconstructed  $R(\theta)$  by the inversion of  $V(z)$  (Liang *et al* 1985).

Quality of adhesion at an interface is a property that it would be very desirable to image by acoustic microscopy. There is some evidence that this may be possible (Bray *et al* 1980; Addison *et al* 1986, 1987). For example, samples were prepared of gold film of 500 nm thickness on a glass substrate, one half of which was first given a 20–30 nm flash of chromium. The chromium interlayer gives better adhesion to the glass. The Rayleigh velocity in the region with the chromium interface was slower by 2% or more and the two regions gave different contrast in an acoustic image (linear elastic perturbation theory would predict an increase in velocity, due to the higher stiffness of the chromium, of a little under 0.2%). It is not altogether clear to what aspect of adhesion the acoustic microscope should be sensitive. Quality of adhesion is an elusive concept, but the strength of an adhesive bond in almost all cases involves fracture behaviour under deformation that is plastic, or, in the case of polymer, viscoelastic. If an acoustic power of 0.1 mW is concentrated in a focal spot of area  $1 \mu\text{m}^2$ , then the amplitude of the normal component of stress in the surface of a high-impedance specimen is 35 MPa. This is relatively small compared with the adhesive strength between most metals, semiconductors and ceramics. And the frequencies in the acoustic microscope are far higher than those of most viscoelastic processes involved in polymer adhesion. So it would seem that the acoustic microscope is sensitive to only those aspects of adhesion that are governed by elastic properties. It is certainly sensitive to the true contact area. If the scale of the loss of contact is much less than the resolution, then the interface will appear as a compliant boundary (Thompson *et al* 1983); this will affect  $V(z)$  and therefore the contrast. On the other hand if the scale



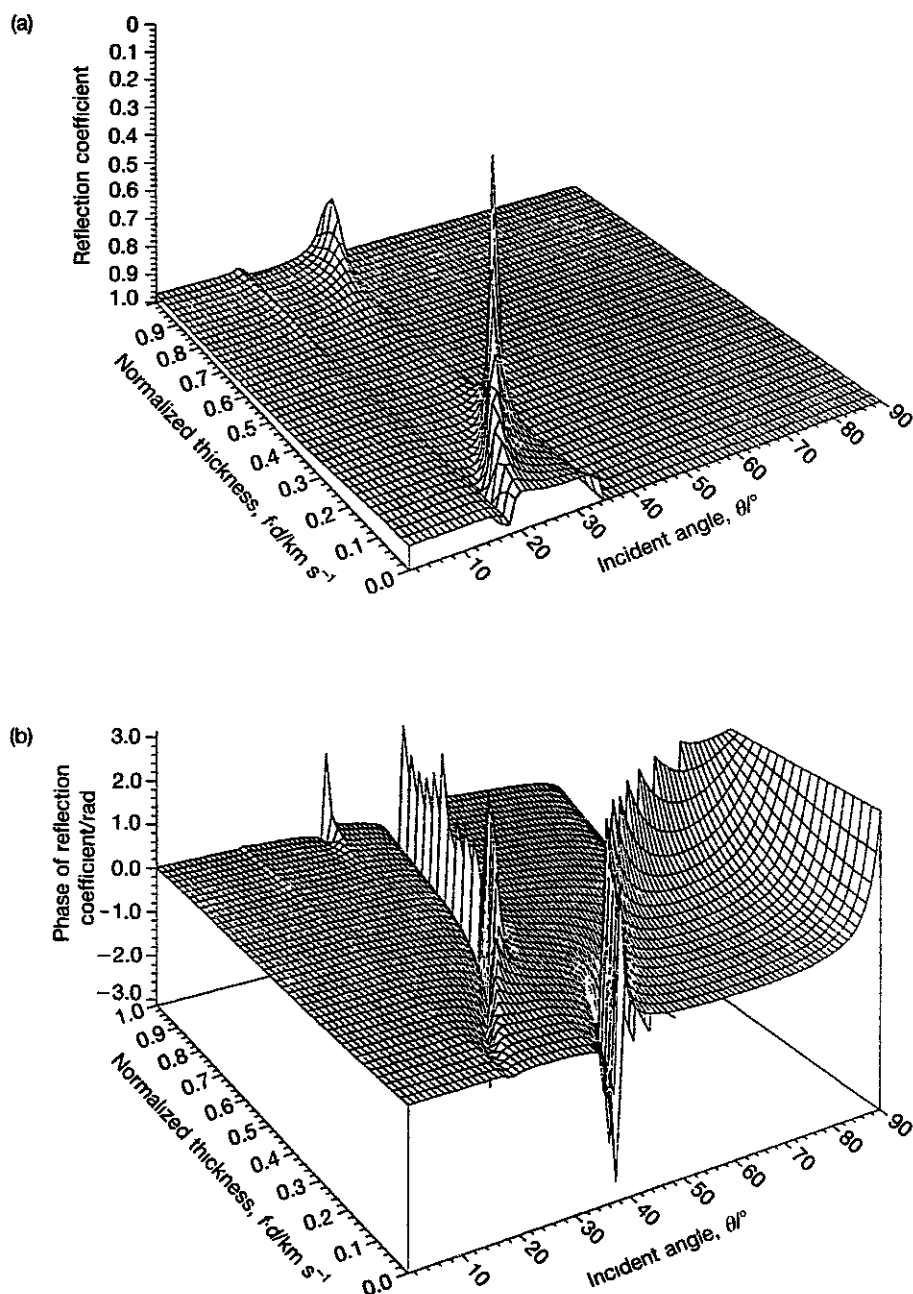


**Figure 15.** Reflectance function for a layer of gold on 42%Ni-Fe alloy as a function of both the incident angle  $\theta$  and the frequency-thickness product  $fd$ : (a) magnitude, plotted as  $1 - |R(\theta)|$  to show the sharp minima in the magnitude, (b) phase (Tsukahara *et al* 1989).

of disbonding is greater than the resolution then the disbonded regions can be imaged directly.

Integrated circuits have been studied fairly extensively by acoustic microscopy, and in addition to disbonding the defects that have been reported also include resist/metal overhang, subsurface blisters and resist inclusions, hillocks shorting between metallization layers, spikes in epi-layers, thickness variations and microcracks. It is frustrating that many of the most interesting high-resolution pictures that have been taken of defects in integrated circuits cannot be published for proprietary reasons, which makes it impossible to discuss them. But it may be that the most important applications of acoustic microscopy to electronic devices are at lower frequencies for inspection of packaging problems.

Just as ultrasonic techniques at conventional non-destructive testing frequencies are invaluable for the inspection of mechanical joints in large structures, so acoustic microscopy can be used to examine bonding to substrates and heatsinks in electronic and optoelectronic structures. Figure 16 shows two acoustic images of an InP laser that was supposed to be gold bonded to a ceramic substrate. Figure 16(a) was taken with the top surface at the focal plane,  $z = 0$ . The large defects at the edge and near the middle are due to handling and the removal of the ball-bonded gold wire that was connected to the top surface. There are some slightly brighter regions in the specimen, but the contrast is not easy to see in this picture. Figure 16(b) was taken at  $z = -180 \mu\text{m}$ . The specimen was about  $80 \mu\text{m}$  thick, and so this defocus probably corresponds to shear waves excited in the solid being focused on the interface. Since shear waves have roughly half the velocity of longitudinal waves they are the first to be focused on an interior plane as the specimen is moved towards the lens, and they also have half the wavelength so that the resolution is correspondingly better. In the defocused image the faint patches in the previous picture show up as strongly reflecting, corresponding to serious disbonds. This specimen was taken from a batch that was giving widely varying lifetimes, some unacceptably short. The disbonds to the heatsink would more than account for the failures, especially as high currents are needed to achieve population inversion of the electrons and the material was known to be liable to thermal degradation. Fascinating pictures of the bonds in so-called flip-chip microelectronic modules have been obtained, through 0.5 mm or so of silicon (Weglein 1983, Tsai and Lee 1987). Indeed, the use of acoustic microscopy techniques to inspection of small components using a lower frequency range (say 20–200 MHz) is an important area of application (Smith *et al* 1985, Burton *et al* 1985, Vettters *et al* 1989), especially in the examination of semiconductor device packaging (Kulik *et al* 1990, Howard 1990, Revay *et al* 1990, Briggs and Hoppe 1991, Moore 1992). Figure 17 shows an area of disbond in an electronic device imaged at 60 MHz.

Figure 18 shows a series of images at even lower frequency, focusing down through the layers of a glass-fibre-reinforced composite. The material had been subject to impact damage, and it is well known that this can seriously effect the structural properties of the composite even when the damage is scarcely visible on the surface. As the microscope focuses from one ply to the next, the damage follows the orientation of the ply. The contrast from each layer is almost completely unclouded by scattering from the layers that precede it, and it is alarming to see how much the damage increases with depth. The loss of signal away from focus has been extensively studied for scanning optical microscopy (Wilson and Sheppard 1984, Boyde 1987, Shotton 1989, Sheppard and Cogswell 1990), and similar analysis can be applied to scanning acoustic microscopy (Heygster *et al* 1990). Indeed, the confocal optical microscope is closely con-

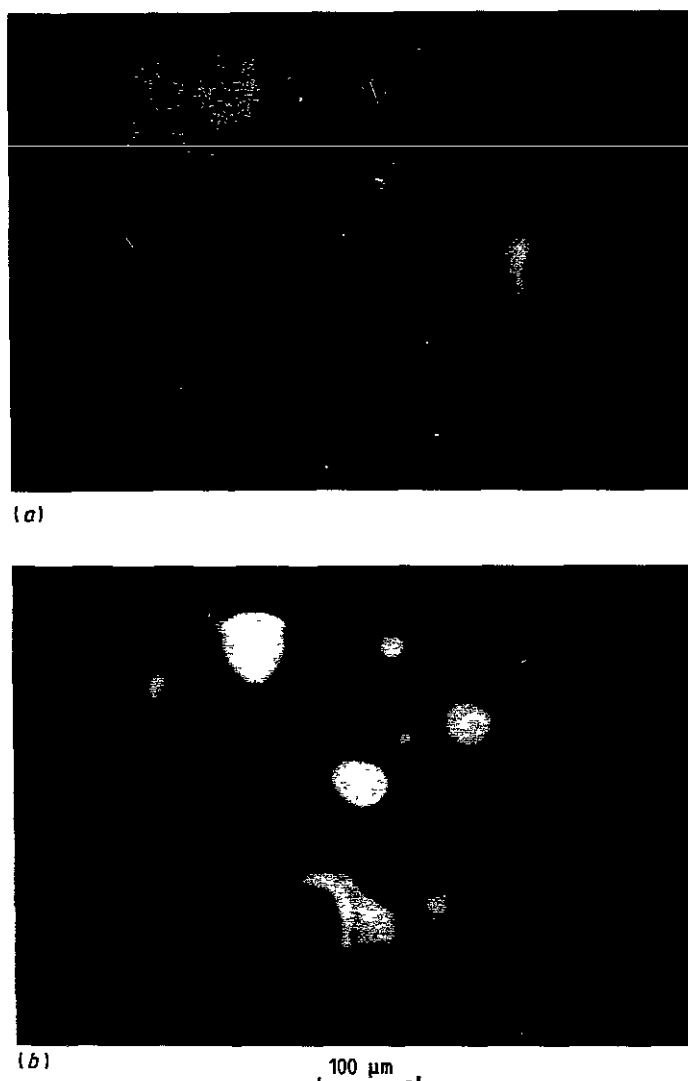


**Figure 16.** An InP laser gold bonded to a ceramic substrate (a)  $z=0$ , (b)  $z=-180\ \mu\text{m}$ , 400 MHz

nected to the acoustic microscope, and both arose out of joint activities between Stanford and Oxford Universities. In conventional microscopes an illuminated point reflector that is out of focus appears dimmer because the light from it is spread over a larger area of the image; but if a whole reflecting plane is out of focus, then provided the illumination does not change it will contribute the same intensity to the image whatever the defocus. In a confocal microscope, the contribution to the brightness of an image from a plane reflector diminishes dramatically away from focus. This effect can be used to enhance the information from subsurface planes.

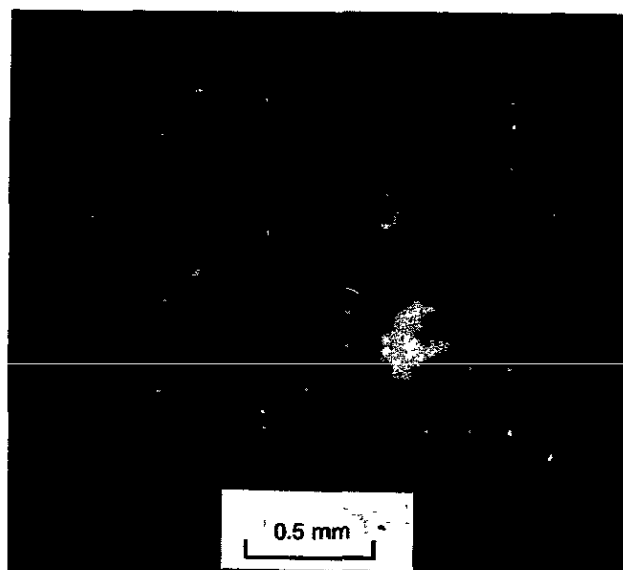


Figure 17. Delamination in a semiconductor device, 60 MHz,  $z = -50 \mu\text{m}$  (Courtesy of Leica, Wetzlar)

In these last examples of subsurface imaging at relatively low frequencies Rayleigh waves have not played a part. Essentially, the defocus has been sufficient to put the surface contributions into the far negative tail of the  $V(z)$  curve, and thus to allow the reflection of subsurface bulk waves to make the major contribution to the signal. This is a digression, albeit an important one, from the main theme that in high-resolution acoustic microscopy of most solids the contrast is dominated by factors that affect the propagation of Rayleigh and other surface waves. This is certainly true of the next two areas of application, the imaging of anisotropy and of surface cracks.

### 3.3. Anisotropy

In the surface of a half-space that is isotropic, the Rayleigh wave velocity is the same in all directions. If the surface is imagined to be in a horizontal plane, then the Rayleigh wave is composed of a shear wave component polarized in a vertical plane (sv) and a longitudinal wave component. Shear waves polarized horizontally (sh) can also exist, but they do not couple to the Rayleigh wave at all (nor, in the case of fluid loading, would they couple into waves in the fluid).

In the surface of an anisotropic solid the situation is more complicated. Pure Rayleigh waves can exist only along certain symmetry directions in which pure sv waves exist. Away from these directions, however, the two quasi-shear polarizations are not pure sv and sh, and, therefore, although the particle motions are orthogonal, at the surface they can be weakly coupled. If the sh mode has a higher velocity than the sv, then there can be no real solution to Snell's law for bulk waves, and the surface wave remains bound to the surface. But if the sh velocity is less than the sv velocity, then a surface wave can couple at the surface itself into waves of orthogonal polarization which can then propagate energy into the bulk. Because such coupling is weak the

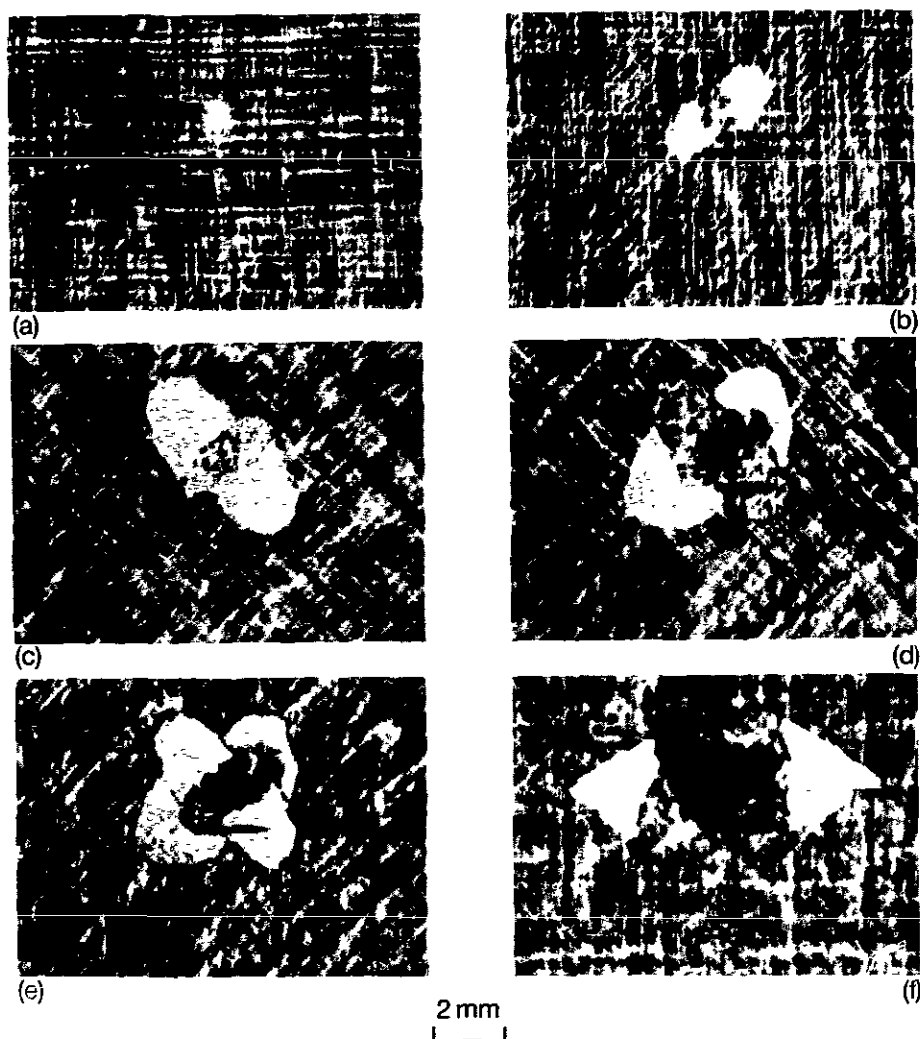
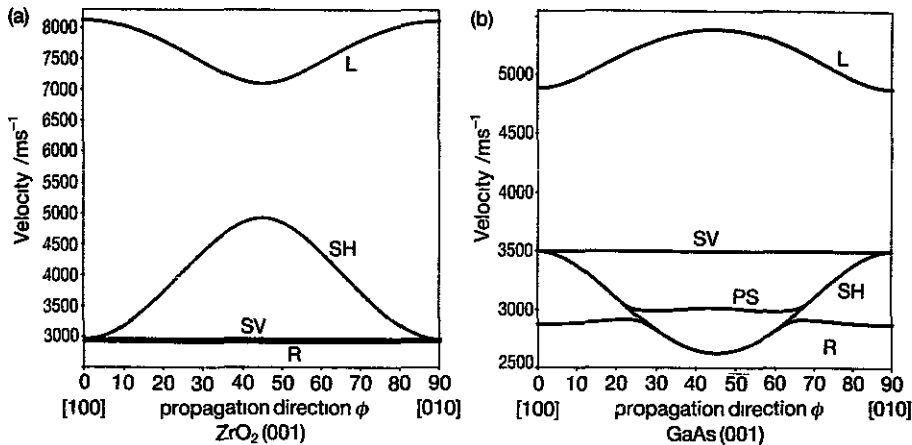


Figure 18. Successive ply layers of a glass-fibre-reinforced composite damaged by impact of a missile from an air-gun, 50 MHz. (Courtesy of Olympus.)

surface wave exists as a recognizable mode, but because its energy becomes gradually depleted it is not a pure surface wave, and so it is designated a pseudo-surface wave (Farnell 1970).

The situation is illustrated for  $\{001\}$  surfaces of two cubic crystals in figure 19. The ratio of shear velocities in a  $\langle 110 \rangle$  direction is  $(v_{sv}/v_{sh})_{\langle 110 \rangle} = A^{1/2}$ , where the anisotropy factor  $A \equiv 2c_{44}/(c_{11} - c_{12})$ . Figure 19(a) illustrates a case where  $A < 1$  and  $v_{sh} > v_{sv}$ ; the particular values used are for cubic zirconia with a small addition of yttria. Although  $v_{sv}$  does not change with angle, the anisotropy in  $v_l$  leads to a small variation in the Rayleigh wave velocity with propagation direction. But there is only one surface wave, and it remains bound to the surface at all angles. Most metals and semiconductors



**Figure 19.** Velocities of bulk and surface waves in an (001) plane, the angle of propagation  $\phi$  in the plane is relative to a (100) direction. (a) zirconia, anisotropy factor  $A = 0.36$ , (b) gallium arsenide, anisotropy factor  $A = 1.83$ ; Bulk polarizations. L, longitudinal; sv, shear vertical, polarized normal to the (001) plane; SH, shear horizontal, polarized in the (001) plane Surface modes: R, Rayleigh, slower than any bulk wave in that propagation direction, PS, pseudo-surface wave, faster than one polarization of bulk shear wave propagating in that direction.

have  $A > 1$ ; their situation is illustrated in figure 19(b), with values corresponding to gallium arsenide. For propagation in the (100) direction, the Rayleigh wave is polarized vertically. As the angle from the (100) direction increases, the polarization remains quasi-vertical until the Rayleigh branch approaches the  $v_{SH}$  curve, when the quasi-shear horizontal mode takes over as the dominant component in the Rayleigh wave, whose polarization therefore twists over towards the horizontal. The Rayleigh velocity remains slightly lower than the bulk SH velocity but becomes indistinguishable from it as the (110) direction is approached, until in the (110) direction it is pure SH and the Rayleigh character has been lost. At directions of propagation other than (110) the Rayleigh wave remains bound to the surface with no leakage of energy into the bulk. Meanwhile, on the other side of the bulk SH curve, and with a velocity close to what the Rayleigh mode would have had if it had not been interrupted by the SH branch, another surface wave has developed. Its polarization is close to the vertical, and it has a character very similar to the Rayleigh wave in the case  $A < 1$ . The difference is, however, that Snell's law has a real solution for SH waves propagating away from the surface into the solid, so the energy is not bound to the surface and the wave is only a pseudo-Rayleigh wave, more commonly known as a pseudo-surface wave. In the (110) direction the coupling of the SH wave to all other modes vanishes, and so the wave becomes pure Rayleigh at the very point at which, for the same reason, the Rayleigh branch disappeared.

If, *per impossibile*, the coupling between modes at the surface could be switched off, there would be two independent waves that could propagate parallel to the surface. One would be Rayleigh in character, and the other quasi-shear horizontal. These two branches would cross each other at the point where they were degenerate. But because there is coupling, two new branches are formed. One starts off pure shear horizontal but, close to the point where degeneracy would have occurred, it twists its polarization

to predominantly sv and follows the PR branch shown, finally ending up as a pure Rayleigh wave at (110). The other branch is the Rayleigh branch, whose polarization starts off purely in the vertical direction and then twists to become quasi-horizontal, ending up as pure horizontal at (110). The two branches are closest to one another where uncoupled degeneracy would have occurred. The profile of the particle displacements is displayed in figure 20. The characteristic depth of the excitation is comparable to the isotropic case, but the presence of transverse motion parallel to the surface is due to the anisotropy, and corresponds to the twisting of the polarization.

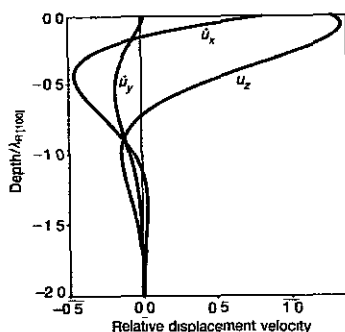


**Figure 20.** Profile of the particle displacement velocities in a Rayleigh wave in a GaAs(001) surface, propagating at an angle  $\phi = 15^\circ$  to a (100) direction. There are components of displacement in both horizontal axes, because of the anisotropy, and so three curves are needed; they have been normalized by setting the larger horizontal component to unity at the surface.

Light fluid loading perturbs the surface wave modes, in general increasing their velocity slightly, but does not alter their basic character as far as propagation into the solid is concerned. In calculating the reflection coefficient and hence  $V(z)$  for anisotropic surfaces, the surface waves are implicit in the equations and it is never necessary to add them in separately. But an understanding of them is invaluable in interpreting the contrast and analysing  $V(z)$  curves. Waves that have a significant component of sv polarization will couple to waves in the fluid, but those that are sh in character will experience vanishingly weak coupling. Other orientations and symmetries will exhibit pseudo-Rayleigh waves in different directions, but the principles remain the same.

A series of reflectance functions for a GaAs(001) surface is shown in figure 21. In each case the modulus of the reflectance function is drawn as a full curve referred to the left ordinate, and its phase is drawn as a broken curve referred to the right ordinate. The angle  $\phi$  is referred to an (010) direction. Figure 21(a) is  $R_{001}(\theta, 0^\circ)$ . Qualitatively it appears quite similar to an isotropic reflectance function, such as the one for fused silica in figure 5(b)i. Point A marks the longitudinal critical angle, where the reflection coefficient is unity. B marks the shear wave critical angle, beyond which no energy can propagate into the solid. C indicates the Rayleigh angle, with its familiar phase change. But even in this symmetry direction, no isotropic material could ever generate this reflectance function (for example, the ratios of longitudinal, shear and Rayleigh velocities would be quite impossible). D indicates the point at which the angle of refraction of the shear wave is  $90^\circ$  (the glitch associated with this is barely visible), in

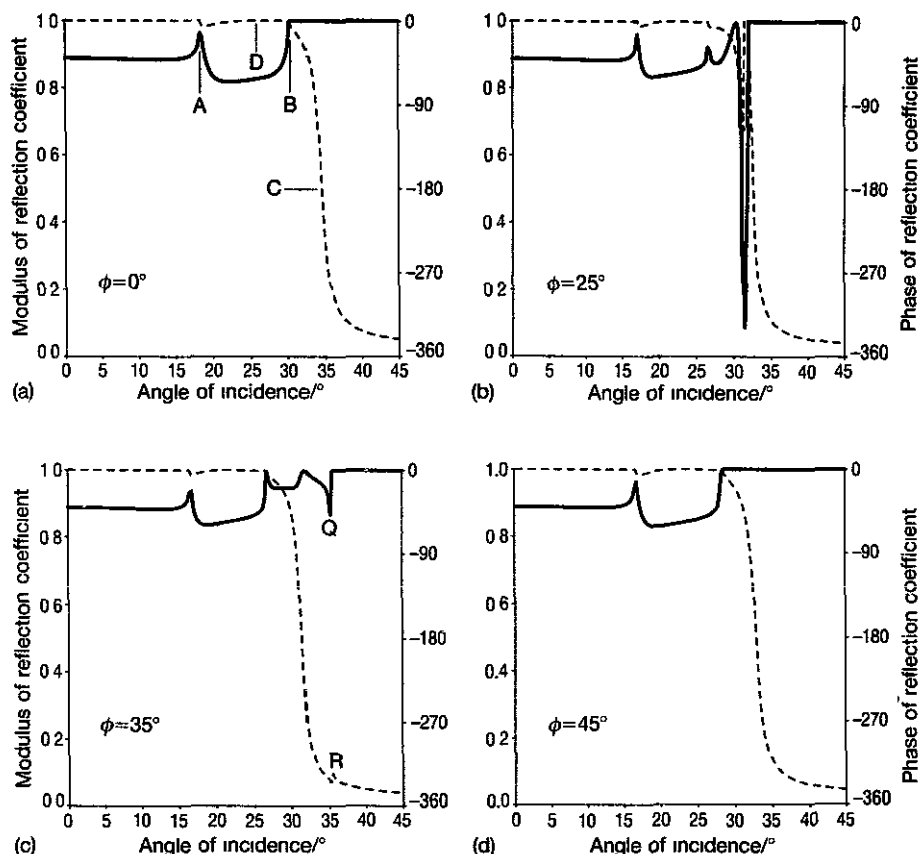


Figure 21. Reflectance functions  $R_{001}(\theta, \phi)$  for GaAs(001) (a)  $\phi = 0^\circ$ , (b)  $\phi = 25^\circ$ ; (c)  $\phi = 35^\circ$ , (d)  $\phi = 45^\circ$ .

an isotropic material this would be the shear critical angle, but because of the reentrant slowness surface the shear critical angle occurs beyond this point. For water/GaAs,  $v_0/\sqrt{(c_{44}/\rho)} = 0.443$ , corresponding to an angle  $\theta_m = 26.3^\circ$ .

At  $\phi = 25^\circ$ , figure 21(b), the effects of anisotropy are more obvious. The modulus becomes unity at the longitudinal critical angle, much as before. It then rises again at the quasi-sv critical angle (about  $27^\circ$ ). At  $\theta = 32^\circ$  the modulus again rises to unity and there is a phase change of a little over  $-\pi/2$ . This corresponds to the excitation of the pseudo-Rayleigh wave. There is a sharp dip in the magnitude to less than 0.1, because at this azimuthal angle the pseudo-Rayleigh wave is quite strongly coupled to the bulk quasi-sh wave, which is slightly slower and can therefore leak energy into the bulk. The quasi-sh critical angle is at  $\theta \approx 32^\circ$ , and this is straddled by the Rayleigh wave phase change of  $-2\pi$ . These phenomena in  $R(\theta, \phi)$  can be correlated with the various modes by following down a vertical locus through  $\theta = 30^\circ$  in figure 19(b), and correlating the mode velocity  $v_m$  with angle via Snell's law for  $90^\circ$  refraction:

$$\sin \theta_m = \frac{v_0}{v_m}. \quad (3.1)$$



At a larger azimuthal angle,  $\phi = 35^\circ$ , figure 21(c), the pseudo-Rayleigh wave has become dominant. The Rayleigh wave has become almost SH in character and is only very weakly coupled to the fluid, so that both the quasi-SH critical angle ( $Q$ ) and the phase change at the Rayleigh angle ( $R$ ) are almost insignificant. In the (110) direction,  $\phi = 45^\circ$ , figure 21(d), the old Rayleigh wave vanishes due to merger into the SH mode, and the old pseudo-Rayleigh wave takes on pure Rayleigh character (not because it is slower than the SH wave, but because at exactly this angle there is no coupling to it).  $R_{001}(\theta, 45^\circ)$  again appears qualitatively like an isotropic reflectance function, but like the  $R_{001}(\theta, 0^\circ)$  curve it could not in fact have been generated by any combination of isotropic elastic constants.

A spherical lens averages over all  $\phi$ , so that the contrast for an anisotropic specimen is (Somekh *et al* 1984)

$$V_{hkl}(z) = \frac{V_0}{2\pi} \int_0^{2\pi} \int_0^{\pi/2} R_{hkl}(\theta, \phi) P(\theta, \phi) e^{i2kz \cos \theta} \sin \theta \cos \theta \, d\theta \, d\phi. \quad (3.2)$$

The integration could be performed by calculating  $V(z)$  for each  $\phi$ , and then integrating over  $\phi$ . Alternatively, a complex mean reflectance function (denoted by prime) may be calculated as

$$R_{hkl}'(\theta) = \frac{1}{2\pi} \int_0^{2\pi} R_{hkl}(\theta, \phi) \, d\phi. \quad (3.3)$$

By swapping the order of integration in (3.2), and assuming axial symmetry of the lens, the contrast may now be written as

$$V_{h',l}(z) = V_0 \int_0^{\pi/2} R_{hkl}(\theta) P(\theta) e^{i2kz \cos \theta} \sin \theta \cos \theta \, d\theta \, d\phi. \quad (3.4)$$

This looks identical in form to the equation for  $V(z)$  in anisotropic material, but  $R_{hkl}'(\theta)$  may be quite different from any isotropic reflectance function. Figure 22 presents theoretical  $V(z)$  curves calculated for Al, Ni and Cu. These represent series of increasingly anisotropic materials, with anisotropy factors:  $A_{Al} = 1.22$ ,  $A_{Ni} = 2.63$ ,  $A_{Cu} = 3.20$ , where  $A = 2c_{44}/(c_{11} - c_{12})$ . Iron has an anisotropy factor  $A_{Fe} = 2.32$ , and ferrous alloys, most notably austenitic stainless steel, exhibit behaviour similar to nickel. For each metal,  $V(z)$  curves are shown for {100}, {110} and {111} surfaces. The curves for Al show strong oscillations associated with the clear phase changes in the complex mean reflectance functions. But because of the weak anisotropy, the three curves do not differ much from one another. The curves for Ni show greater differences from each other, with  $V_{100}(z)$  differing more from the other two than they differ from each other. In copper the oscillations in  $V(z)$  are very weak and, despite the strong anisotropy, there is little difference between the three curves. Or rather, it may be partly because the strong anisotropy causes the range of angles over which the phase change is averaged to be so great that extensive cancellation occurs and, except in the {100} orientation, the oscillations to be so weak. In any case, the large angles characteristic of copper mean that the reflections of interest occur at angles where the lens response is relatively weak. Although grains have been imaged in polished but not etched specimens of aluminium (Weaver 1986, Fossheim *et al* 1988) and copper (Bray 1981), in both cases the contrast was rather poor. But nickel and iron and related alloys such as stainless steel, and also many ceramics, can give excellent grain contrast.

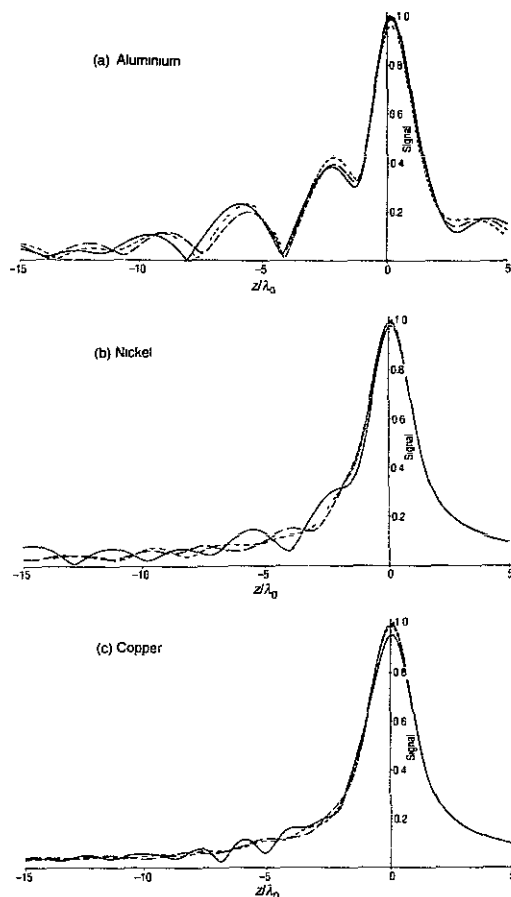


Figure 22.  $V(z)$  curves calculated from complex mean reflectance functions (a) Al; (b) Ni, (c) Cu, with orientations — (100), --- (110), - - - (111).

Images of a polycrystalline specimen of nickel are presented in figure 23. At focus,  $z = 0$  (figure 23(a)), there is little contrast, though grain boundaries can just be detected. At  $z = -4 \mu\text{m}$  (figure 23(b)), the contrast between grains is much better. At  $z = -7 \mu\text{m}$  (figure 23(c)), the contrast is even stronger, but contrast reversal has occurred. Of course, it is most unlikely that these grains had exact symmetrical crystallographic orientations but, in order to discuss the interpretation of the contrast and its relation to the  $V(z)$  curves in figure 22, suppose that the grains  $\alpha$ ,  $\beta$  and  $\gamma$  had orientations lying close to {110}, {100} and {111}, respectively. At focus, the  $V(z)$  curves from all three orientations coincide. No contrast would be expected here, and little is found in figure 22(a). At defocus  $z = -4 \mu\text{m}$ , the {100} curve shows a smaller signal than the other two, so that it would appear darker in an image. A {111} grain would be slightly darker than a {110} grain, but the difference is much smaller. At  $z = -7 \mu\text{m}$  defocus, complete reversal of the contrast would be expected. The  $V(z)$  curve for {100} now indicates that this should be the darkest. These observations can be compared with what is seen in the pictures. Using a directional point-focus lens it is possible to invert



Figure 23. Polycrystalline nickel (a)  $z = 0$ , (b)  $z = -4 \mu\text{m}$ , (c)  $z = -7 \mu\text{m}$ , 0.73 GHz (Somekh *et al* 1984).

the process in order to identify the approximate crystallographic orientation of grains from analysis of directional  $V(z)$  measurements (Hildebrand and Lam 1983, Kushibiki *et al* 1989). Even with a conventional spherical lens it is possible, with accurate analysis, to identify specific velocity components in  $V(z)$ , because beam-steering effects can deflect all but the surface waves travelling in symmetry directions away from a return path to the transducer. For example, in measurements on  $Y$ -cut  $\alpha$ -quartz at 225 MHz ( $r_0 = 0.75 \text{ mm}$ ), the Fourier transform of  $V(z)$  data from an axially symmetric spherical point-focus lens showed three well-defined peaks corresponding to 3147, 3395 and  $3878 \text{ m s}^{-1}$  (Kushibiki *et al* 1989).

The calculation of  $V(z)$  curves such as in figure 22 for anisotropic surfaces is considerably more difficult than in the isotropic case, because of the need to sum the reflectance function over all angles in order to find the complex mean, and to solve Snell's law numerically for each value of  $\theta$  and  $\phi$  (there is no analytic solution in the anisotropic case). But, once again, it is found that waves propagating in the surface play a key role. This is why the best contrast from grain structure, and indeed from most other variations in elastic properties, is found with negative defocus,  $z < 0$ .

It would be marvellous to be able to image plastic deformation by acoustic microscopy, for example around the tip of a crack. Acoustic waves can be attenuated by

dislocations that are associated with plastic deformation of crystalline materials (Granato and Lücke 1966). The dislocations act like violin strings in treacle; they are overdamped and, in trying to respond to the stresses associated with passing elastic waves in the solid, they dissipate energy from the waves through interactions with thermal phonons. But the mechanism is largely confined to materials in which the Peierls stress is small, and that largely means face-centred-cubic metals. The two chief candidate materials for model experiments are copper and aluminium. Many of the original dislocation damping experiments were performed on single crystals of 99.999% pure copper. But, as figure 22 suggests, it is difficult to couple into surface waves in copper in an acoustic microscope. Aluminium is much more promising. There is strong coupling to Rayleigh waves, and the low anisotropy factor means that in a polycrystalline specimen the picture would be less cluttered with grain and grain boundary contrast. But even with 99.999% pure aluminium the experiment is not easy. The activation energy for point defect creation and migration is relatively low in aluminium, and at the temperatures at which good acoustic microscopy measurements with water coupling can be made, any dislocation damping following plastic deformation is quenched in a matter of minutes by point defects pinning the dislocations (Weaver and Briggs 1985).

There is one experiment in which plastic deformation seems undoubtedly to have been captured (Ishikawa *et al* 1989). Figure 24 shows a specimen of an Fe-3%Si alloy that has been deformed. Every precaution was taken to eliminate spurious sources of contrast; for example, the specimen was carefully repolished after deformation to avoid any topographical contrast due to bowing in or out of the surface around a stress concentrator as a result of deformation under plane strain. So the contrast seems indubitably to be due to interaction of Rayleigh waves with regions of plastic deformation. But the mechanism of the contrast in this picture has never been satisfactorily explained. The solubility of Si in Fe is low, as indeed it is in many metals, and so it is possible that the dislocations are not pinned too much by solution hardening. But

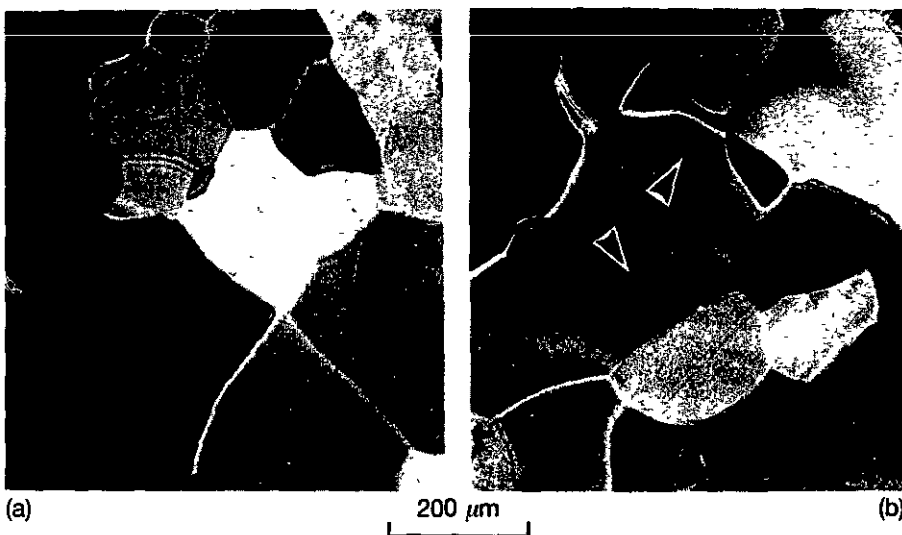


Figure 24. Fe-3%Si alloy, before and after deformation (Courtesy of Hitachi)

the experience with pure metals raises at least a cautionary flag. Fe-Si alloys are widely used for transformer cores, and they exhibit twinning under plastic deformation. It may be that the contrast is due to twinning on a scale too small to be resolved, but which through the microscopic alternation of anisotropy causes significant perturbation and scattering of Rayleigh waves.

It would be unthinkable not to include a picture of a high- $T_c$  superconductor, and so a picture of  $\text{YBa}_2\text{C}_3\text{O}_{7-x}$  is given in figure 25. The difficulties in preparing such a specimen and protecting it from degradation under water are formidable. Twin structure is faintly visible in some of the grains, and as the defocus was varied in the microscope so the boundaries between adjacent grains became more apparent. In some pictures of grain structure the grain boundaries seem to have a contrast of their own, quite distinct from the grains on either side. The theory presented for grain contrast so far cannot account for this; it would suggest that the transition from the contrast of one grain to the next should simply be gradual over a distance of about the resolution. In order to understand the grain boundary contrast it is necessary to have a theory of contrast from discontinuities in a surface.

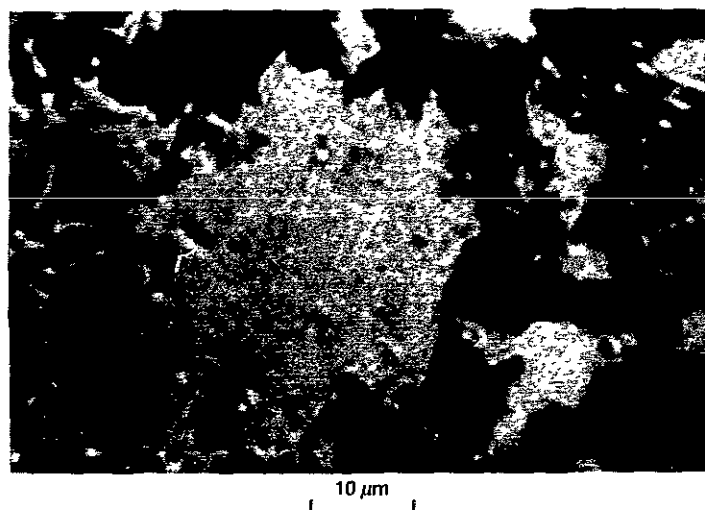


Figure 25. High  $T_c$  superconductor ceramic,  $\text{YBa}_2\text{C}_3\text{O}_{7-x}$ , hot pressed, 1.7 GHz (Buckney *et al* 1990).

### 3.4. Surface cracks and boundaries

A plain bearing made of an experimental Al-20%Si alloy was subjected to a fatigue test and then examined for incipient fatigue cracks. The pictures in figure 26 are optical and acoustic images of a section through the bearing. Figure 26(a) is an optical image taken with a 10x objective. The bearing alloy is in the centre with a steel substrate on the left. No doubt with higher magnification and etching it might be possible to find the cracks. But with no further preparation the acoustic image of the same area at the same magnification (figure 26(b)) is able to reveal the cracks with greatly enhanced contrast because of the Rayleigh wave scattering mechanism. In many pictures of

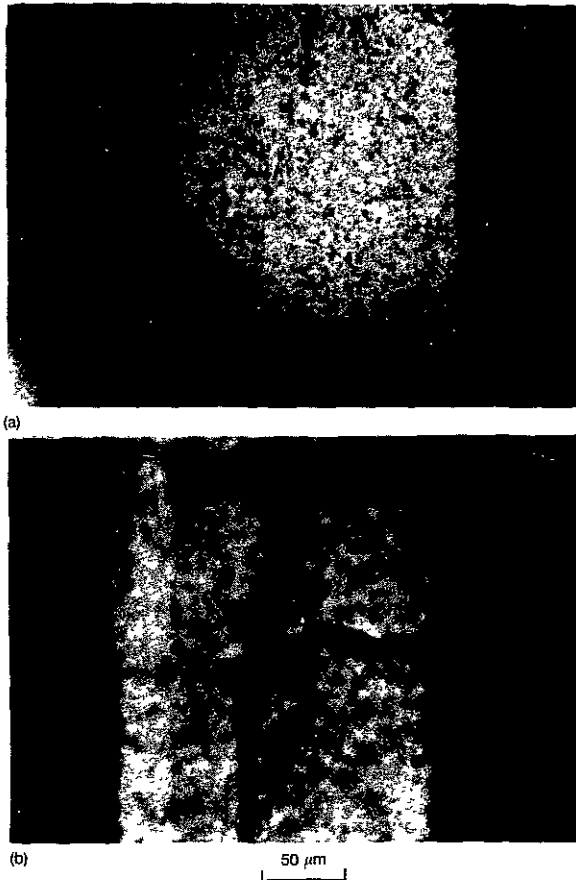


Figure 26. Incipient fatigue cracks in an experimental Al-20%Si plain bearing alloy (a) optical, 10 $\times$  objective, (b) 0.73 GHz (Ilett *et al* 1984)

cracks, such as those in figures 10 and 11, there are fringes of separation half a Rayleigh wavelength. The mechanism for these fringes can be seen by imagining a Rayleigh ray in the specimen in figure 7 to be reflected by a crack so that it travels back to the lens along its original path. As the lens is scanned sideways, the phase of the ray reflected by the crack will change by  $2\pi$  when the path changes by  $\lambda_R$ , and therefore when the lens moves by an amount  $\lambda_R/2$ . The path of the axial ray will be constant as the lens scans parallel to the surface, and so the interference between the Rayleigh ray and the axial ray will undergo a complete cycle for a sideways displacement of the lens by  $\lambda_R/2$ , giving rise to fringes of that spacing in the image.

The presence of a crack or other discontinuity presents a serious difficulty for the standard  $V(z)$  theory, because the reflectance function is defined for infinite plane waves that are reflected into infinite plane waves, and this requires a reflecting surface that is uniform. If a surface contains a crack then this requirement is violated, and an incident plane wave may be scattered into a whole family of waves (Tew *et al* 1988). This scattering can be described in  $k$ -space by a scattering function  $S(k_c, k'_c)$ , where

the prime refers to incident waves and the unprime to scattered waves. The  $x$ -direction is taken as tangential to the surface, the  $z$ -direction normal to the surface and at this stage the theory is confined to two dimensions in the plane normal to both the surface and the crack. The response of the microscope can then be written in terms of the scattering function by integrating over the incident and reflected waves separately,

$$V(x, z) = \int_{-k_0}^{k_0} \int_{-k_0}^{k_0} \exp[i(k'_z - k_z)z] L_1(k'_x) L_2(k_x) S(k_x, k'_x) \times \exp[i(k'_x - k_x)x] dk_x dk'_x \quad (3.5)$$

where  $k'_z = \sqrt{[(\omega/v_0)^2 - k'^2_x]}$ ,  $k_z = \sqrt{[(\omega/v_0)^2 - k^2_x]}$  are taken as negative and positive respectively,  $L_1(k'_x)$ ,  $L_2(k_x)$  are the lens functions for outgoing and incoming waves, and the crack is taken to be at the origin. Thus, the first term of the integrand allows for phase shifts due to defocus, and the last term allows for phase shifts due to lateral displacement of the lens from the position directly above the crack. It can be seen that in the absence of a crack, when  $S(k_x, k'_x)$  vanishes except at  $k_x = k'_x$ , the expression reduces to the simple formula for  $V(z)$ . The problem now is to find  $S(k_x, k'_x)$ .

The key to calculating the scattering function is to recognize that the fringes so often seen in pictures of cracks confirm that once again Rayleigh waves are responsible for the contrast. Indeed, if a crack is very fine, so that it is much less than a wavelength wide at the surface, then the geometrically reflected waves must bounce off the surface almost oblivious of the crack. Therefore the trick is to separate the reflectance function into the geometrical part and the Rayleigh part in the way shown in (2.23), and then to let the geometrical reflection occur as if there were no crack, and let the Rayleigh part be scattered by the crack as the Rayleigh ray propagates in the surface. This requires a certain amount of Fourier transforming between the descriptions of the incident and scattered fields as functions of wavevector components, and the reflection by the crack which must be described as a function of position. Eventually the scattering function is found to be

$$S(k_x, k'_x) = R_0(k_x) \delta(k_x - k'_x) + \frac{2\alpha_R}{\pi} \times \left( \frac{(T_R - R_R - 1)k_x k'_x + (T_R + R_R - 1)k_p^2}{(k_x^2 - k_p^2)(k'^2_x - k_p^2)} \right). \quad (3.6)$$

The first term on the right-hand side describes the reflection in the absence of a crack. The second term represents the scattering due to the crack. A crack that has  $T_R = 1$  and  $R_R = 0$  has no effect, and in that case this term vanishes. But any other combination of  $T_R$  and  $R_R$  allows this term to contribute, and to scatter waves into different values of  $k_x$ . Because this is a Rayleigh wave effect, this term contributes most when both the incident wave and the scattered wave are close to the Rayleigh angle (where  $\alpha_R$  is the measure of what is meant by close).

There are several approximations in the derivation of (3.6). First, it assumes that Rayleigh wave scattering mechanisms dominate the contrast. Second, it assumes that the fluid loading is light, i.e.  $\alpha_R \ll k_R$ . Third, the effect of the crack on the geometrical reflection is neglected. There may well be other terms. The theory of lateral wave crack contrast can be tackled along the lines introduced in section 2.4.1. In anisotropic materials pseudo-surface waves can be excited, and it might well be possible to

incorporate these in the model. But for the large number of cases where the dominance of the Rayleigh wave contrast is confirmed by the experimental evidence of Rayleigh wave fringes parallel to a crack, or simply Rayleigh periodicity in  $V(z)$  of the material, then the theory presented here seems to be useful. In slower materials, where lateral waves are important, the theory could be adapted using the separation of (2.25) and (2.26).

The values of  $R_R$  and  $T_R$  to be used in the expression for  $S(k_x, k'_x)$  are external to the theory presented here. This has the great advantage that the large library of solutions for different configurations of cracks (e.g. Achenbach 1987), each of which may be a major computational exercise in itself, can be drawn on for the particular crack configuration of interest. These solutions are generally for Rayleigh waves from infinity incident on cracks in free surfaces, in the absence of any fluid loading. In the use of these for contrast from cracks in the acoustic microscope it should be appreciated that there will be a perturbation due to the fluid loading. Also, because of the exponential attenuation of leaky Rayleigh waves they cannot be generated at infinity; indeed, in the microscope they may be generated very close to the crack. As with the ray calculation of  $V(z)$  on a uniform surface, therefore, this calculation of crack contrast may be expected to work best when the defocus is not too small.

The form of the three-dimensional scattering function can be obtained by substituting  $k_p^2 - k_y^2$  for  $k_p^2$ , to give the correct Rayleigh pole behaviour, and multiplying by an extra factor  $k_p/\sqrt{(k_p^2 - k_y^2)}$ . The Cartesian coordinate system is extended to three dimensions, with the crack lying in the plane  $x = 0$ , and the component of the wavevector parallel to the crack  $k_y$ . Since the crack is continuous along its length, the component  $k_y$  parallel to the crack must be conserved in any reflection from the crack, and therefore throughout the problem. The three-dimensional scattering factor is then

$$S(k_x, k'_x, k_y) = R(\theta)\delta(k_x - k'_x) + \frac{2\alpha_R}{\pi} \times \left( \frac{(T_R - 1 - R_R)k'_x + (T_R - 1 + R_R)(k_p^2 - k_y^2)}{(k_x^2 + k_y^2 - k_p^2)(k_x'^2 + k_y^2 - k_p^2)} \right) \frac{k_p}{\sqrt{k_p^2 - k_y^2}}. \quad (3.7)$$

In this expression  $T_R$  and  $R_R$  refer to Rayleigh waves propagating obliquely to the crack, i.e. with phase variation  $\exp[ik_y y]$  along  $y$ . The first term on the right is simply the reflectance function for a defect-free surface (with  $\theta = \cos^{-1}(k_x/k)$ ). The second term describes departures from this due to the presence of the crack. It is explicit in this formalism that  $S(k_x, k'_x, k_y)$  is a function not only of  $k_x$  and  $k'_x$ , but also of  $k_y$ . This dependence occurs through the dependence of  $T_R$  and  $R_R$  on the angle of incidence  $\phi$  of the Rayleigh wave (Angel and Achenbach 1984). Those results are for excitation of the Rayleigh waves at infinity, in which case the angles of transmission and reflection in the surface by a uniform crack must each be equal to the angle of incidence. In the acoustic microscope, excitation is not from infinity, and therefore  $k_x$  and  $k'_x$  are not necessarily the same; indeed, this was the basis of the derivation of  $S(k_x, k'_x)$ . But the available calculations of  $T_R(\phi)$  and  $R_R(\phi)$  are undefined when  $k_x \neq k'_x$ . To overcome this difficulty the further approximation can be made that, provided that  $T_R(\phi)$  and  $R_R(\phi)$  do not vary too rapidly with angle of incidence of the Rayleigh wave, they may be written as functions of  $k_y$  only, by putting  $\phi = \sin^{-1}(k_y/k)$ . In most cases this will be a good approximation, since although formally  $k_x$  and  $k'_x$  are each summed indepen-



dently between  $\pm k_y$ , in fact there is significant contribution to the sum only when they are both close to  $\sqrt{(k_p^2 - k_y^2)}$ .

In order to calculate  $V(x, z)$  for a spherical lens in the presence of a crack a summation must be made over  $k_y$ . For each value of  $k_y$ , a double summation is first made over  $k_x$  and  $k'_x$ . A wave is considered to be incident with components of wavevector  $k'_x$  and  $k_y$ . It is then transmitted by the crack with components of wavevector  $k_x$  and  $k_y$ , and reflected also with components  $k_x$  and  $k_y$ ; transmitted and reflected waves may be summed in the same integral. If the axis of the lens is displaced a distance  $x$  from the crack, the resulting phase change is  $k'_x x$  for the incident wave and  $-k'_x x$  for the scattered wave. Then, by extension of (3.5),

$$V(x, z) = \int_{-k}^k \int_{-k}^k \int_{-k}^k \exp[i(k'_x + k_x)z] L_1(k'_x, k_y) L_2(k_x, k_y) S(k_x, k'_x, k_y) \times \exp[i(k'_x - k_x)x] dk_x dk'_x dk_y. \quad (3.8)$$

This gives the contrast due to a crack in a specimen in an imaging acoustic microscope for any defocus and lens position. Once again a great advantage of expressing the result in this form, with  $T_R$  and  $R_R$  as external parameters in the Green function, is that when different geometries are encountered, such as varying depth or partial crack closure, solutions independently obtained for those situations may be incorporated directly. There is active development of the theory of contrast from cracks and subsurface features along these and other lines (Howe 1991, Rebinsky and Harris 1992a, b, Veom *et al* 1992).

The use of a line scan display on an acoustic microscope enables the theory to be tested directly. In figure 27, images are presented of a crack from an indent in glass. Superimposed on each image are lines scans, or  $V(x)$ , measured along the white line across-the-middle of each picture. Beside each picture is a line scan calculated using the two-dimensional theory, calculated using the values (Achenbach *et al* 1980)

$$\begin{aligned} T_R &= 0 \\ R_R &= 0.4 \exp(i 0.6). \end{aligned} \quad (3.9)$$

Comparison with the three-dimensional theory remains to be made, but the agreement between the two-dimensional theory and the measurements is not too bad, and suggests that the two-dimensional theory does indeed give a useful account of what is going on.

The theory also predicts a number of phenomena that are often encountered experimentally. The Rayleigh fringes have already been discussed, and they can be seen to arise immediately from the term  $\exp[i(k'_x - k_x)x]$  in (3.5). Reversal of the macroscopic contrast is often found, and again this can be seen in the calculated curves in figure 27. Perhaps most important of all, the theory is based entirely on the assumption that the crack has no effect on the geometrical reflection. This means that the crack can be as fine as you like and still give contrast, provided that Rayleigh waves incident on it experience some scattering. Extensive investigations confirm that indeed there seems to be no surface crack that is too fine to be seen by acoustic microscopy (Briggs *et al* 1990). Cracks in a range of materials, from glass to zirconia, give fringes parallel to the crack that extend all the way to its very tip. If the contrast were somehow proportional to the separation of the crack walls, then it would gradually diminish towards the tip, but that is not what happens. Indeed, the tip itself seem to be an acoustically well-defined feature, so that in suitable contrast conditions circular fringes

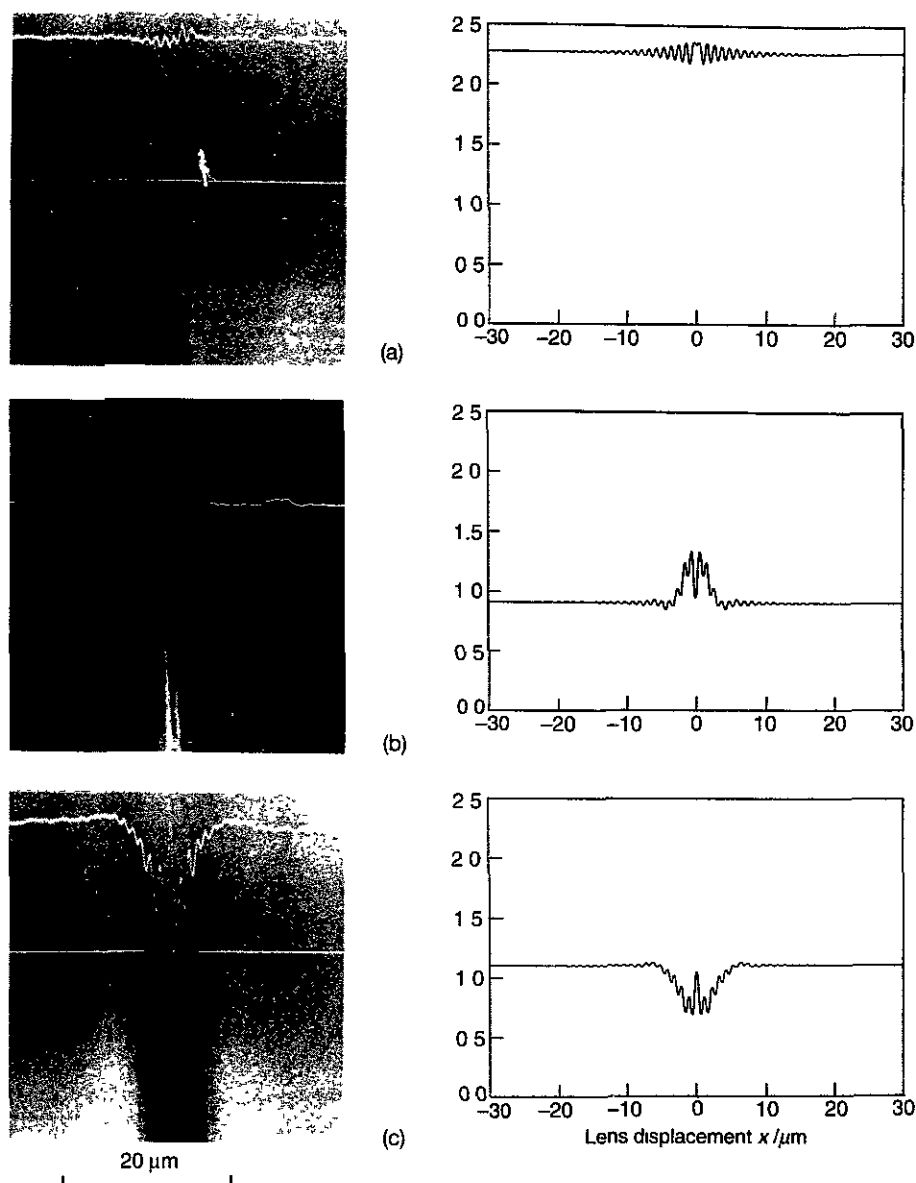


**Figure 27.** A crack from an indent in glass (a)  $z = 0 \mu\text{m}$ , (b)  $z = -3.8 \mu\text{m}$ , (c)  $z = -5.2 \mu\text{m}$ , FLSAM, 1.5 GHz. The experimental line-scans superimposed on the images can be compared with the plots calculated using two-dimensional theory (12.2), (12.13) and (12.14) with values of defocus (a)  $z = 0 \mu\text{m}$ , (b)  $z = -4.2 \mu\text{m}$ , (c)  $z = -6.8 \mu\text{m}$ . The values of  $z$  in the calculations were chosen for best fit, the reason for the discrepancy is not known, though no doubt there are the usual uncertainties associated with thermal drift, the measurement of  $z$  and the frequency and pupil function used (Briggs *et al* 1990).

are seen, centred on the tip of the crack. No doubt with suitable image analysis such fringes could be used to give subwavelength measurements of the cracklength.

There are, presumably, two ways in which cracks could be too small to measure. One is if the crack is smaller than a wavelength in more than one dimension. By dimensional arguments similar to those that Lord Rayleigh originally used to explain why the sky is blue, a deep defect of characteristic dimension  $a$  laterally, such as a deep drilled hole of radius  $a$ , would give a scattered intensity proportional to  $a^4/\lambda_R^3$ . A defect near the surface that was characterized by  $a$  in all three dimensions, such as a near surface void of radius  $a$ , would give a scattered intensity proportional to  $a^6/\lambda_R^5$ . Such strong wavelength dependence would give sensitive means of characterizing subsurface damage by multifrequency methods. The other way that a crack could be too small to measure is if the walls are so close together that there is transmission of not only normal stress between the faces, but shear stress as well. In a liquid of viscosity  $\eta_0$ , and density  $\rho_0$ , at a frequency  $\omega$  the amplitude of a shear wave decays by a factor  $e$  over a distance

$$d_e = \sqrt{(2\eta_0/\rho_0\omega)}. \quad (3.10)$$

At 1 GHz in water at 20 °C this gives a value of 18 nm, falling to half that value at 2 GHz and 60 °C. In many situations, asperity contact would be more important at that separation.

In the grinding of brittle materials, multiple abrasion by fine particles creates an array of vertical surface cracks of surprisingly uniform depth, and also causes plastic flow to occur so that near the surface the faces of the cracks are in compression. These cracks with closed mouths are elastically equivalent to cracks normal to the surface but starting some way below it. Rayleigh wave scattering coefficients for such geometries are available, and their frequency dependence has features that are determined both by the total depth of the crack, and by the extent of the crack closure at the mouth (Achenbach and Brind 1981). This effect has been used to investigate the nature of machining damage in brittle materials by measuring the reflection of Rayleigh waves; the test material was hot-pressed silicon nitride, chosen because it is free from stress corrosion cracking at room temperature and also because it is such an important structural ceramic (Tien *et al* 1982, Marshall *et al* 1983). Such measurements have been extended to imaging grinding damage, again in hot-pressed silicon nitride, by acoustic microscopy (Clarke *et al* 1985). There were two particularly interesting aspects of the experiments. The first arose from the frequency dependence of the scattering from subsurface cracks. Pictures were taken over a range of frequencies from 25 to 60 MHz, and amazingly enough the distribution of crack geometries was sufficiently small to enable systematic differences to be seen: in one specimen the picture at 35 MHz was almost blank, corresponding to a crack depth of 35  $\mu\text{m}$  with the top 7  $\mu\text{m}$  or so of the crack faces in contact. Second, it was found that by blanking off 180° of the lens, and also the central portion of the aperture, the microscope could be operated in a dark field mode, so that only backward scattered Rayleigh waves contributed any signal. Scans made with this lens gave a significantly greater level of contrast and were therefore somewhat easier to interpret.

The scattering function of (3.6) can be extended to the more general case of different materials on either side of the boundary; indeed, it was originally derived in that form (Somekh *et al* 1985). The two sides are denoted by subscripts 1 and 2, having Rayleigh wavenumbers  $k_{p1}$  and  $k_{p2}$  with imaginary components  $\alpha_1$  and  $\alpha_2$ . Transmission and reflection coefficients  $T_{R1}$ ,  $T_{R2}$  and  $R_{R1}$ ,  $R_{R2}$  are defined for waves incident from sides

1 and 2, respectively. Then the scattering function becomes

$$\begin{aligned}
 S(k_x, k'_x) = & R_0 \delta(k_x - k'_x) + i2\delta(k_x - k'_x) \left( \frac{\alpha_1 k_{p1}}{k_x^2 - k_{p1}^2} + \frac{\alpha_2 k_{p2}}{k_x'^2 - k_{p2}^2} \right) \\
 & + \frac{1}{2\pi} \left[ 2\sqrt{\alpha_1 \alpha_2} \left( \frac{T_{R2}}{(k_x + k_{p1})(k'_x + k_{p2})} + \frac{T_{R1}}{(k_x - k_{p2})(k'_x - k_{p1})} \right) \right. \\
 & - \frac{2\alpha_1}{k_x + k_{p1}} \left( \frac{1}{k'_x + k_{p1}} + \frac{R_{R1}}{k'_x - k_{p1}} \right) \\
 & - \frac{2\alpha_2}{k_x - k_{p2}} \left( \frac{1}{k'_x - k_{p2}} + \frac{R_{R2}}{k'_x + k_{p2}} \right) \\
 & \left. + \frac{4}{k'_x - k_x} \left( \frac{\alpha_1 k_{p1}}{k_x^2 - k_{p1}^2} - \frac{\alpha_2 k_{p2}}{k_x'^2 - k_{p2}^2} \right) \right]. \quad (3.11)
 \end{aligned}$$

The Green function can be used in (3.5) to calculate the contrast in the vicinity of a boundary between two different materials. Like the two-dimensional theory for cracks, this may be used to help understand the contrast that is seen at boundaries. Once again the values of the reflection and transmission coefficients are external to the theory. A Rayleigh impedance can be defined as the Rayleigh velocity multiplied by the density and, in cases where the difference in Rayleigh impedance across the boundary is not too great, approximate values for the Rayleigh wave transmission and reflection coefficients can be taken as

$$\begin{aligned}
 T_{R1} &= \frac{2Z_2}{Z_2 + Z_1} & T_{R2} &= \frac{2Z_1}{Z_2 + Z_1} \\
 R_{R1} &= -R_{R2} = \frac{Z_2 - Z_1}{Z_2 + Z_1}. \quad (3.12)
 \end{aligned}$$

If calculations are performed for a boundary between hypothetical materials that have different Rayleigh velocities, and whose impedances can be varied, then the difference in the real parts of  $k_p$  on either side of the crack can give strong contrast at the boundary even in the absence of scattering, i.e. even when  $T_1 = T_2 = 1$ ,  $R_1 = R_2 = 0$ . Where the lens straddles the boundary the path taken by the Rayleigh ray corresponds neither to one material by itself nor the other. It has a Rayleigh angle for one material on one side of the boundary and to the other on the other side. Thus a  $V(z)$  scan over the boundary would have a periodicity intermediate between the periodicity of each material by itself. In  $V(x)$  this manifests itself as oscillations of periodicity not  $\pi/k_R$ , but  $2\pi/(k_{R1} - k_{R2})$ . This periodicity exists only for a range of  $x$  such that a Rayleigh wave that is excited in one material is detected after it has crossed the boundary and reradiated from the other. Self-evidently this effect cannot occur at positive defocus.

The model can be used to give an approximate indication of the contrast to be expected at grain boundaries. In this case the density of the material is the same on both sides of the boundary, but because of the crystal anisotropy and the different orientations of adjacent grains the velocities and polarizations of surface waves either side of a grain boundary will be different. In some cases the crystal anisotropy is so great that fringes are seen parallel to the grain boundaries, a notable example being zirconia which has a crystal anisotropy greater than almost any other common ceramic (Ingel and Lewis 1988). But generally the scattering of surface waves at grain boundaries is considerably less than at cracks. This gives a useful way to distinguish between boundaries and cracks. Figure 28(a) shows an image of a stainless steel specimen that has been subject to fatigue. It is difficult to find the fatigue cracks, because they are

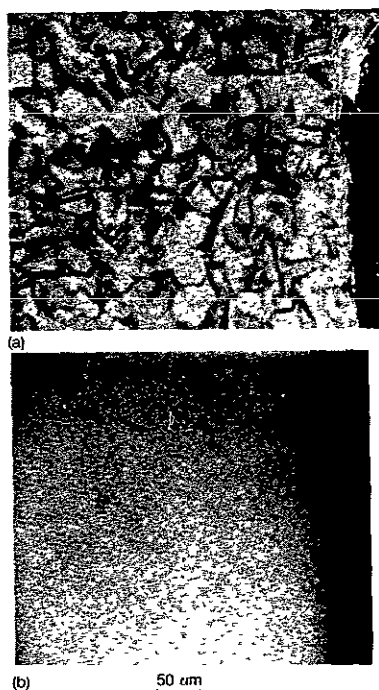


**Figure 28.** Short incipient fatigue cracks in stainless steel: (a) negative defocus, (b) positive defocus (Rowe *et al* 1986).

camouflaged against the grain boundaries. But the contrast mechanisms have different dominant contributions. The chief mechanism for contrast from the cracks is the scattering of surface waves by the crack, whereas the chief contribution to contrast from the grain boundaries is the change of surface wave propagation parameters from one grain to the next. Contrast that depends on the change in Rayleigh angle across a boundary will be present only at negative defocus. On the other hand, contrast that depends on reflection of surface waves from a crack will be present at zero and positive defocus (with a central dead zone of width approximately  $2z \tan \theta_R$ ). Thus, by using positive defocus it should be possible to distinguish small fatigue cracks from grain boundaries. This is illustrated in figure 28(b), where the cracks do indeed appear with a small dead zone and Rayleigh fringes either side. By studying how the contrast varies with defocus it is possible to distinguish between different kinds of elastic discontinuity that give contrast in the acoustic microscope. It may even be possible to identify persistent slip bands and relate them to crack nucleation and growth at the earliest stages of fatigue (Jenkins 1990, Zhai *et al* 1990). The aim would be to be able to measure the detailed geometrical and interfacial parameters of cracks and boundaries from comparisons between experiment and theory.

Figure 29 is a picture of a silicon carbide fibre (Nicalon) in a calcium–aluminosilicate glass matrix. This picture is taken from a detailed study of a large number of ceramic matrix, glass–ceramic matrix, and metal matrix composites (Lawrence 1990). The interface between the fibre and the matrix is not where it appears at first sight to be.

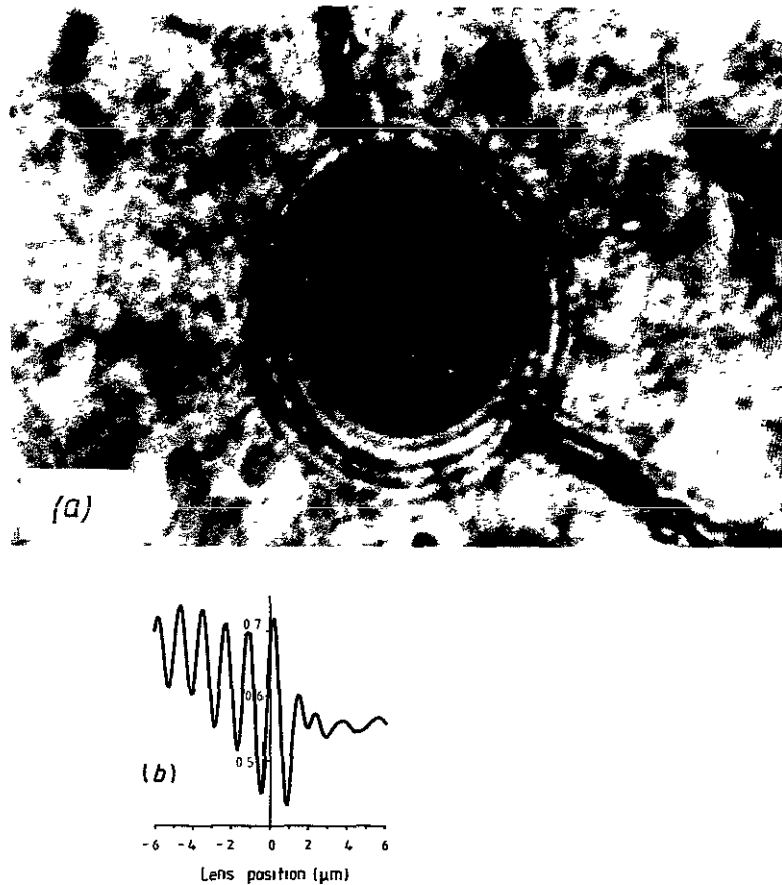


**Figure 29.** A silicon carbide fibre in a calcium-aluminosilicate glass matrix: (a) ELSAM, 1.9 GHz,  $z = -3.2 \mu\text{m}$ , (b) calculated contrast from (12.2), (12.42) and (12.43), this time the experimental parameters gave the best fit without any adjustment! (Lawrence 1990)

Starting from the middle of the fibre, there are a few Rayleigh fringes with a rather dark mean background, then the mean level becomes brighter and there are four or five fringes before they fade further out into the matrix. But the interface is not where the average contrast changes from dark to bright, it is one or two fringes further out than that. A clue to this is where the fringes from a crack in the matrix stop. The inset shows a calculation of a line scan across a boundary between these two materials. The material constants of the matrix and the fibre were used to calculate approximate transmission and reflection coefficients from (3.12);  $V(x)$  was then calculated for the frequency and defocus used in figure 29, and plotted with the same horizontal scale for direct comparison. In the calculated curve, not only do the mean levels vary in about the right way, but the big oscillations in  $V(x)$  continue to the right of the boundary just as the fringes do in the picture.

#### 4. Where next?

The key message of acoustic microscopy is that it enables the interaction of acoustic

waves with elastic properties and features to be visualized with microscopic resolution. In solids, a dominant role is often played by Rayleigh waves and other surface waves, and the dependence of their velocity on bulk properties and anisotropy and surface layers. There is especially strong sensitivity to scattering by surface cracks and boundaries. At lower resolutions, and in polymeric materials, Rayleigh waves are less dominant, and useful interior imaging is possible. This can bridge the gap between high-resolution acoustic microscopy and conventional NDT, and the enhanced depth discrimination of a confocal system can be exploited.

For many applications, it is desirable to be able not only to image the interaction of acoustic waves with the specimen, but to measure them too (Briggs *et al* 1988, 1992). For example, since there is a Fourier relationship between the reflectance function of a surface and the  $V(z)$  curve of the acoustic microscope, it is possible to invert the Fourier transform to deduce  $R(\theta)$  (Liang *et al* 1985). The Fourier transform is a complex-valued relationship, and so it is necessary to know both the amplitude and the phase of  $V(z)$  (Liang *et al* 1986). If these cannot be measured, then phase retrieval methods can be used to deduce  $R(\theta)$  (Fright *et al* 1989). When such reconstructions of  $R(\theta)$  are performed, the feature that invariably stands out most clearly with stiff materials is the angle of the Rayleigh wave phase change. This is not surprising if the strongest interaction with the surface is the excitation of Rayleigh waves. In that case, rather than trying to measure the whole reflectance function (up to the angle of the lens), it may be better to be more specific and concentrate on a measurement of the Rayleigh wave parameters (i.e. the velocity and attenuation) alone. In the simplest form these can be measured from any  $V(z)$  curve by measuring the period and decay of the Rayleigh oscillations. But much more sophisticated methods have been developed, of which the best established is the line-focus-beam technique (Kushibiki and Chubachi 1985), in which a cylindrical lens is used, with its axis parallel to the surface of the specimen, to generate Rayleigh waves in one direction only in the surface of the specimen. Anisotropic specimens, such as wafers of electronic materials, can therefore be studied, in all the richness of the phenomena described in section 3.3 (Kushibiki *et al* 1991a, b). In its original form, the line-focus-beam sacrificed spatial resolution in order to achieve angular resolution, but micro-line-focus-beam lenses are now being made that give good angular and spatial resolution. Lenses are being developed for other key specialized applications: a conical lens is available that can be tuned to excite waves in a structure with a thin surface layer, this can give exceptional sensitivity to any changes in the thickness or adhesion of the layer, and  $V(f)$  measurements enable the observations to be quantified (Atalar and Köymen 1987, 1989). A microspectrometer has been developed that allows measurement of anisotropic layered specimens by measuring the frequency dependence of the reflection as a function of angle (Tsukahara *et al* 1989). Thin layers can also be measured by time-resolved acoustic microscopy; resolution of echoes from surfaces less than  $2\text{ }\mu\text{m}$  apart is possible (Wang *et al* 1990). Time-resolved measurements are being used to measure the depth of short cracks at the early stages of fatigue in alloys, with a resolution better than 5% in cracks of length  $\mu\text{m}$  or so (Knauss *et al* 1992). What such techniques make possible, whether they are  $V(z)$  or  $V(f)$  or time-resolved measurements, is quantitative interpretation of what one can learn from the interaction of acoustic waves with the elastic properties of a specimen in an acoustic microscope.

#### Acknowledgments

I am deeply grateful to all the colleagues and friends, in Oxford and internationally,

who have contributed ideas and results. I am also grateful to Oxford University Press for allowing me to use figures from the monograph *Acoustic Microscopy* (1992), in which further details of many of the topics discussed here will be found.

## References

- Achenbach J D 1987 Flaw characterisation by ultrasonic scattering methods *Solid Mechanics Research For Quantitative Non Destructive Evaluation* ed J D Achenbach and Y Rajapakse Dordrecht Nijhoff pp 67-81
- Achenbach J D and Brind R J 1981 Scattering of surface waves by a sub-surface crack *J. Sound Vibration* **76** 43-56
- Achenbach, J D, Gautesen A K and Mendelsohn, D A 1980 Ray analysis of surface-wave interaction with an edge crack *IEEE Trans SU-27* 124-9
- Addison R C, Somekh M G and Brigs G A D 1986 Techniques for the characterisation of film adhesion *IEEE 1986 Ultrasonics Symp.* 772-82
- Addison R C, Somekh M G, Rowe J M and Briggs G A D 1987 Characterisation of thin-film adhesion with the scanning acoustic microscope *Pattern Recognition and Acoustical Imaging SPIE* **768** 275-84
- Angel Y C and Achenbach J D 1984 Reflection and transmission of obliquely incident Rayleigh waves by a surface breaking crack *J. Acoust Soc Am* **75** 313-39
- Ash E A and Paige E G S (eds) 1985 *Rayleigh-Wave Theory and Applications* (Berlin: Springer)
- Atalar A 1978 An angular spectrum approach to contrast in reflection acoustic microscopy *J. Appl. Phys* **49** 5130-9
- 1979 A physical model for acoustic signatures *J. Appl. Phys* **50** 8237-9
- Atalar A and Hoppe M 1986 A high performance acoustic microscope *Rev. Sci. Instr.* **57** 2568-76
- Atalar A and Köymen H 1987 Use of a conical axicon as a surface acoustic wave focussing device *IEEE Trans UFFC-34* 53-63
- 1989 A high efficiency Lamb wave lens for subsurface imaging *IEEE 1989 Ultrasonics Symp.* 813-6
- Attal J 1980 Acoustic microscopy with liquid metals *Scanned Image Microscopy* (London: Academic) pp. 97-118
- Attal J and Quate C F 1976 Investigation of some low ultrasonic absorption liquids *J. Acoust Soc Am* **59** 69-73
- Attal J, Saïed A, Saurel J M and Ly C C 1989 Acoustic microscopy deep focusing inside materials at gigahertz frequencies *Acoustical Imaging* **17** 121-30
- Auld B A 1973 *Acoustic Fields and Waves in Solids* (New York: Wiley)
- Auld B A 1985 Rayleigh wave propagation *Rayleigh Wave Theory and Applications* ed E A Ash and E G S Paige (Berlin: Springer) pp 12-28
- Bertoni H L 1984 Ray-optical evaluation of  $V(z)$  in the reflection acoustic microscope *IEEE Trans. SU-31* 105-16
- Bertoni H L and Tamir T 1973 Unified theory of Rayleigh angle phenomena for acoustic beams at liquid-solid interfaces *Appl. Phys* **2** 157-72
- Bjørnø L and Lewin P A 1986 Measurement of nonlinear acoustic parameters in tissue *Tissue Characterization with Ultrasound* ed J F Greenleaf vol 1 (Boca Raton: CRC Press) pp 141-63
- Born M and Wolf E 1980 *Principles of Optics: Electromagnetic Theory of Propagation, Interference and Diffraction of Light* (Oxford: Pergamon)
- Boyde A 1987 Colour-coded stereo images from the tandem scanning reflected light microscope (TSRLM) *J. Microsc.* **146** 137-42
- Bracewell R N 1978 *The Fourier Transform and its Applications* (New York: McGraw-Hill)
- Bray R C 1981 Acoustic and photoacoustic microscopy *Ph D Thesis Ginzton Lab. Report 3243* Stanford University
- Bray R C, Quate C F, Calhoun J and Koch R 1980 Film adhesion studies with the acoustic microscope *Thin Solid Films* **74** 295-302
- Briggs G A D 1992 *Acoustic microscopy* (Oxford: Oxford University Press)
- Briggs G A D and Hoppe M 1991 *Acoustic Microscopy Images of Materials* ed D B Williams, A R Pelton and R Gronsky (New York: Oxford University Press)
- Briggs G A D, Jenkins P J and Hoppe M 1990 How fine a surface crack can you see in a scanning acoustic microscope? *J. Microsc.* **159** 15-32



- Briggs G A D, Rowe J M, Sinton A M and Spencer D S 1988 Quantitative methods in acoustic microscopy *IEEE 1988 Ultrasonics Symp.* 743–9
- Buckney M A, Chernosatonskii L A and Maev R G 1990 Acoustic imaging of high-temperature superconducting materials *J. Microsc.* **160** 299–313
- Burton N J, Thaker D M and Tsukamoto S 1985 Recent developments in the practical and industrial applications of scanning acoustic microscopy *Ultrasonics Int* **85** 334–8
- Chan K H and Bertoni H L 1990 Ray-optical representation of longitudinal lateral waves in acoustic microscopy *IEEE Trans. UFFC* **38** 27–34
- Chiznik D 1991 Quantitative acoustic microscopy for measurement of material properties *Ph.D. Thesis* Polytechnic University of New York
- Chubachi N 1985 Ultrasonic microspectroscopy via Rayleigh waves *Rayleigh-Wave Theory and Applications* ed E A Ash and E G S Paige (Berlin: Springer) pp 291–7
- Clarke L R, Chou C -H, Khuri-Yakub B T and Marshall D B 1985 Acoustic evaluation of grinding damage in ceramic materials *IEEE 1985 Ultrasonics Symp.* 979–82
- Dransfeld, K and Salzmann E 1970 Excitation, detection and attenuation of high-frequency elastic surface waves *Physical Acoustics* vol VII ed W P Mason and R N Thurston (New York: Academic) pp 260–83
- Farnell G W 1970 Properties of elastic surface waves *Physical Acoustics* vol VI ed W P Mason and R N Thurston (New York: Academic) pp 109–66
- Farnell G W and Adler E L 1972 Elastic wave propagation in thin layers *Physical Acoustics* vol IX ed W P Mason and R N Thurston (New York: Academic) pp 35–127
- Fosshelm K, Bye T, Sathish S and Heggum G 1988 Acoustic scanning microscopy of grain structure in isotropic solids pure aluminium and Al–2.5%Mg alloy *J. Mater. Sci.* **23** 1748–51
- Foster J S and Rugar D 1983 High resolution acoustic microscopy in superfluid helium *Appl. Phys. Lett.* **42** 869–71
- 1985 Low-temperature acoustic microscopy *IEEE Trans.* **SU-42** 139–51
- Fright W R, Bates R H T, Rowe J M, Spencer D S, Somekh M G and Briggs G A D 1989 Reconstruction of the complex reflectance function in acoustic microscopy *J. Microsc.* **153** 103–17
- Granato A V and Lucke K 1966 The vibrating string model of dislocation damping *Physical Acoustics* vol IV A ed W P Mason (London: Academic) pp 225–76
- Hadimioglu B and Foster J S 1984 Advances in superfluid helium acoustic microscopy *J. Appl. Phys.* **56** 1976–80
- Hadimioglu B and Quate C F 1983 Water acoustic microscopy at suboptical wavelengths *Appl. Phys. Lett.* **43** 1006–7
- Heiserman J 1980 Cryogenic acoustic microscopy *Scanned Image Microscopy* ed E A Ash (London: Academic) pp 71–96
- Heygster G, Block H, Gadomski A and Boseck 1990 Modeling of the optical transfer function (OTF) of the scanning acoustic microscope (SAM) and its relation to the other scanning microscopes *Optik* **85** 89–98
- Hildebrand J A and Lam L 1983 Directional acoustic microscopy for observation of elastic anisotropy *Appl. Phys. Lett.* **42** 413–15
- Hildebrand J A, Liang K and Bennett S D 1983 Fourier-transform approach to material characterization with the acoustic microscope *J. Appl. Phys.* **54** 7016–19
- Howard A M 1990 Evaluation of large die attach using acoustic microscopy *IEE Colloquium on 'NDT Evaluation of Electronic Components and Assemblies'* p 3
- Howe M S 1991 On the image of a cylindrical inclusion in the scanning acoustic microscope *Proc. R. Soc. A* **435** 393–403
- Ilett C, Somekh M G and Briggs G A D 1984 Acoustic microscopy of elastic discontinuities *Proc. R. Soc. London A* **393** 171–83
- Ingel R P and Lewis D 1988 Elastic anisotropy in zirconia single crystals *J. Am. Ceram. Soc.* **71** 265–71
- Ishikawa I, Semba T, Kanda H, Katakura K, Tani Y and Sato H 1989. Experimental observation of plastic deformation areas, using an acoustic microscope *IEEE Trans. UFFC* **36** 274–9
- Jenkins P J 1990 Scanning acoustic microscopy of persistent slip bands. *EMAG-MICRO '89. Proc. of the Institute of Physics Electron Microscopy and Analysis Group and Royal Microscopical Society Conference* ed P J Goodhew and H Y Elder vol 1 pp 153–6
- Jipson V B 1979 Acoustic microscopy of interior planes *Appl. Phys. Lett.* **35** 385–7
- Jipson V B and Quate C F 1978 Acoustic microscopy at optical wavelengths *Appl. Phys. Lett.* **32** 789–91
- Karaki K, Saito T, Matsumoto K and Okuda Y 1991 Nonlinear resolution improvement and second-harmonic generation of a pressurized superfluid <sup>4</sup>He acoustic microscope *Appl. Phys. Lett.* **59** 908–10
- Kino G S 1987 *Acoustic waves: devices, imaging and analog signal processing* (Englewood Cliffs, NJ: Prentice-Hall)

- Knauss D, Bennink D D, Zhai T, Briggs G A D and Martin J W 1992 Depth measurement of short cracks with an acoustic microscope *J. Mater. Sci.* in press
- Kulik A, Gremaud G and Satish S 1990 Acoustic microscopy as a polyvalent tool in materials science *Trans. R. Microsc. Soc.* 1
- Kushibiki J and Chubachi N 1985 Material characterization by line-focus-beam acoustic microscope *IEEE Trans. SU-32* 189-212
- Kushibiki J, Chubachi N and Tejima E 1989. Quantitative evaluation of materials by directional acoustic microscope *Ultrasonics Int.* 89 736-43
- Kushibiki J, Maehara H and Chubachi N 1981 Acoustic properties of evaporated chalcogenide glass films *Electron. Lett.* 17 322-3
- Kushibiki J, Takahashi H, Kobayashi T and Chubachi N 1991a Quantitative evaluation of elastic properties of  $\text{LiTaO}_3$  crystals by line-focus-beam acoustic microscopy *Appl. Phys. Lett.* 58 893-5
- 1991b Characterization of  $\text{LiNbO}_3$  crystals by line-focus-beam acoustic microscopy *Appl. Phys. Lett.* 58 2622-4
- Lawrence C W 1990 Acoustic microscopy of ceramic fibre composites *D. Phil. Thesis* Oxford University
- Lemons R A and Quate C F 1979 Acoustic microscopy *Physical Acoustics* vol XIV ed W P Mason and R N Thurston (London: Academic) pp 1-92
- Liang K K, Bennett S D and Kino G S 1986 Precision phase measurements with short tone burst signals in acoustic microscopy *Rev. Sci. Instr.* 57 446-52
- Liang K K, Kino G S and Khuri-Yakub B 1985 Material characterisation by the inversion of  $V(z)$  *IEEE Trans. SU-32* 213-24
- Marshall D B, Evans A G, Khuri-Yakub B T, Tien J J W and Kino G S 1983 The nature of machining damage in brittle materials *Proc. R. Soc. London A* 385 461-75
- Moore T M 1992 C-mode acoustic microscopy applied to integrated circuit package inspection *Solid State Electron.* 35 41-21
- Muha M S, Moulthrop A A, Kozlowski G C and Hadimoglu B 1990 Acoustic microscopy at 15.3 GHz in pressurized superfluid helium *Appl. Phys. Lett.* 56 1019-21
- Negishi K and Ri H U 1987 Propagation of multi-mode ultrasonic pulses in non-destructive material evaluation *Ultrasonic Spectroscopy and its Application to Materials Science* ed Y Wada (Japan: Ministry of Education, Science and Culture) pp 70-4
- Parmon W and Berton H L 1979 Ray interpretation of the material signature in the acoustic microscope *Electron. Lett.* 15 684-6
- Peck S D and Briggs G A D 1987 The caries lesion under the scanning acoustic microscope *Adv. Dent. Res.* 1 50-63
- Quate C F, Atalar A and Wickramasinghe H K 1979 Acoustic microscopy with mechanical scanning: a review *Proc. IEEE* 67 1092-1114 (reprinted in Lee H and Wade G 1986, *Modern Acoustical Imaging* (New York: IEEE) pp 180-202)
- Rayleigh J W S 1885 On waves propagating along the plane surface of an elastic solid *Proc. London Math. Soc.* 17 4-11 (reprinted in 1903 *Scientific Papers by Lord Rayleigh* vol IV (Cambridge: University Press) and 1964 (New York: Dover Publications))
- Rebinsky D A and Harris J G 1992a An asymptotic calculation of the acoustic signature of a cracked surface for the line focus scanning acoustic microscope *Proc. R. Soc. A* 436 251-65
- 1992b The acoustic signature for a surface-breaking crack produced by a point focus acoustic microscope *Proc. R. Soc.* in press
- Revay L, Lindblad G and Lind L 1990 IC package defects revealed by scanning acoustic microscopy (SAM) *CERT '90, Components Engineering, Reliability and Test Conference (Electron. Components Inst.)* pp 115-22
- Rodriguez-Rey A, Briggs G A D, Field T A and Montoto M 1990 Acoustic microscopy of rocks *J. Microsc.* 160 21-9
- Rowe J M, Kushibiki J, Somekh M G and Briggs G A D 1986 Acoustic microscopy of surface cracks *Phil. Trans. R. Soc. London A* 320 201-14
- Scruby C B, Jones K R and Antoniazzi L 1987 Diffraction of elastic waves by defects in plates *J. NDE* 5 145-56
- Sheppard C J R and Cogswell C J 1990 3-D image formation in confocal microscopy *J. Microsc.* 159 179-94
- Sheppard C J R and Wilson T 1981 Effects of high angles of convergence on  $V(z)$  in the scanning acoustic microscopy *Appl. Phys. Lett.* 38 858-9
- Shotton D M 1989 Confocal scanning microscopy and its applications for biological specimens *J. Cell Sci.* 94 175-206
- Smith I R, Harvey R A and Fathers D J 1985 An acoustic microscope for industrial applications *IEEE Trans. SU-32* 274-88

- Somekh M G, Bertoni H L, Briggs G A D and Burton N J 1985 A two-dimensional imaging theory of surface discontinuities with the scanning acoustic microscope *Proc. R. Soc. London A* **401** 29–51
- Somekh M G, Briggs G A D and Ilett C 1984 The effect of anisotropy on contrast in the scanning acoustic microscope *Phil. Mag.* **49** 179–204
- Tew R H, Ockendon J R and Briggs G A D 1988 Acoustical scattering by a shallow surface-breaking crack in an elastic solid under light fluid loading *Recent Developments in Surface Acoustic Waves* ed D F Parker and C A Maugin (Berlin: Springer) pp 309–16
- Thompson R B, Skillings B J, Zachary L E, Schmerr L W and Buck O 1983 Effects of crack closure on ultrasonic transmission *Review of Progress in Quantitative Nondestructive Evaluation* vol 2 ed D O Thompson and D E Chimenti (New York: Plenum) pp 325–43
- Tien J J W, Khuri-Yakub B T, Kino G S, Evans A G and Marshall D B 1982 Long wavelength measurements of surface cracks in silicon nitride *Review of Progress in Quantitative Nondestructive Evaluation* vol 1 ed D O Thompson and D E Chimenti (New York: Plenum) pp 569–71
- Tsai C S and Lee C C 1987 Nondestructive imaging and characterizations of electronic materials and devices using scanning acoustic microscopy *Pattern Recognition and Acoustical Imaging SPIE* **768** 260–6
- Tsukahara Y, Nakaso N, Kushibiki J and Chubachi N 1989 An acoustic micrometer and its application to layer thickness measurements *IEEE Trans. UFFC* **36** 326–31
- Tsukahara Y, Takeuchi E, Hayashi E and Tan Y 1984 A new method of measuring surface layer-thickness using dips in angular dependence of reflection coefficients *IEEE 1984 Ultrasonics Symp* 992–6
- Veom S A, Harris J G and Achenbach J D 1992 Numerical-analysis of the acoustic signature of a surface-breaking crack *IEEE Trans. UFFC* **39** 112–18
- Vetters H, Matthaei A, Schulz A and Mayr P 1989 Scanning acoustic microprobe analysis for testing solid state materials *Mat. Sci. Eng. A* **122** 9–14
- Wang J, Gundle R and Briggs G A D 1990 The measurement of acoustic properties of living human cells *Trans. R. Microsc. Soc.* **1** 91–94
- Weaver J M R 1986 The ultrasonic imaging of plastic deformation *D. Phil. Thesis* Oxford University
- Weaver J M R and Briggs G A D 1985 Acoustic microscopy techniques for observing dislocation damping *J. Phys.* **12 C10** 743–50
- Weglein R D 1979 A model for predicting acoustic materials signature *Appl. Phys. Lett.* **34** 179–81
- 1983 Integrated circuit inspection via acoustic microscopy *IEEE Trans. SU* **30** 40–2
- Weglein R D and Wilson R G 1978 Characteristic materials signature by acoustic microscopy *Electron. Lett.* **14** 352–4
- Wickramasinghe H K 1978 Contrast in reflection acoustic microscopy *Electron. Lett.* **14** 305–6
- 1979 Contrast and imaging performance in the scanning acoustic microscope *J. Appl. Phys.* **50** 664–72
- Wickramasinghe H K and Petts C R 1980 Gas medium acoustic microscopy *Scanned Image microscopy* ed E A Ash (London: Academic) pp 57–70
- Wilson T and Sheppard C J R 1984 *Theory and Practice of Scanning Optical Microscopy* (London: Academic)
- Yamanaka K, Nagata Y and Koda T 1989 Low temperature acoustic microscopy with continuous temperature control *Ultrasonics Int.* **89** 744–9
- Zhai T-G, Lin S and Xiao J-M 1990 Influence of non-geometric effect of PSB on crack initiation in aluminium single crystal *Acta Metal. Mater.* **38** 1687–92